THE TOP QUARK, OTHER NEW PHENOMENA OBSERVED AT THE CDF IN $p\bar{p}$ COLLISIONS AT $\sqrt{s} = 1.96$ TeV

V. B. Flyagin, J. A. Budagov, V. V. Glagolev, I. A. Suslov

Joint Institute for Nuclear Research, Dubna

THE TOP QUARK, OTHER NEW PHENOMENA OBSERVED AT THE CDF IN $p\bar{p}$ COLLISIONS AT $\sqrt{s} = 1.96$ TeV

V. B. Flyagin, J. A. Budagov, V. V. Glagolev, I. A. Suslov

Joint Institute for Nuclear Research, Dubna

Upgraded Tevatron luminosity in Run II (started 2001) has opened a new level of modern heavy-quark studies compared to that of Run I. Now top event samples contain hundreds of event statistics for investigation. This review mainly covers the mass measurements of the top quark produced at $\sqrt{s} = 1.96$ TeV in $p\bar{p}$ collisions at the Collider Detector of Fermilab (CDF) with the integrated luminosity samples up to 1 fb^{-1}. As an example of the top-quark mass measurements we consider the so-called Matrix Element Method in «lepton + jets» and «dilepton» channels of the top-quark decay. The CDF top-quark mass obtained in «lepton + jets» mode is the world most precise single measurement of this important physics parameter. The review summarizes the essential results of the CDF top-quark mass measurement achieved and published for the recent 2003–2008 period. We consider also b-quark baryon discoveries like $\Sigma_b, \Sigma_b^*, \Xi_b$ as well as first observation of $B_S - \bar{B}_S$ oscillations. Let us mention here that a CDF/JINR group created significant contribution to the new CDF complex and physics investigation.

Возросшая светимость модернизированного тэватрона во втором сеансе открыла новые возможности более совершенного изучения тяжелых кварков: исследования проводятся уже на статистике сотен событий и составили новое направление — физику топ-кварков. В обзоре рассматриваются измерения массы топ-кварков, рожденных в протон-антипротонных взаимодействиях при энергии $\sqrt{s} = 1{,}96$ ТэВ на установке CDF (FNAL) при накопленной светимости ~ 1 фб$^{-1}$. Обзор посвящен в основном измерениям массы топ-кварка с помощью так называемого метода «матричного элемента», дающего наилучшие точности в канале распада топ-кварка «лептон + струи» и в «двухлептонном» канале. Измерение массы топ-кварка на CDF в канале «лептон + струи» является на данный момент наиболее точным отдельным измерением этого важного физического параметра. Работа суммирует наиболее весомые результаты измерения массы топ-кварка на установке CDF, полученные и опубликованные в период 2003–2008 гг. Рассмотрены также открытия барионов, содержащих b-кварк: $\Sigma_b, \Sigma_b^*, \Xi_b$, и первые наблюдения осцилляций $B_S - \bar{B}_S$. Отметим здесь, что группа CDF/JINR внесла существенный вклад в новый комплекс CDF и в физические исследования.

INTRODUCTION

The most important discovery made at the Tevatron, undoubtedly, was the first observation of the top quark, the weak isospin partner of the bottom quark (Table 1). Top quark is the last of the fundamental constituents of subnuclear matter that theories of all kind of interactions and a wealth of experimental information had led particle physicists to expect.

Table 1. **The b- and t-quarks quantum numbers**

Symbol	$I(J^P)$	Charge	Flavour
b	$0\,(1/2^+)$	$-1/3$ e	-1
t	$0\,(1/2^+)$	$2/3$ e	$+1$

Top quark for the first time was observed in $p\bar{p}$ collisions by CDF and D∅ collaborations in 1995 [1].

During Run I operation from 1992 to 1995, CDF acquired 110 pb^{-1} of data at a center-of-mass energy of 1.8 TeV, and performed the first measurements of top-quark properties. The upgraded Tevatron is expected to operate at least through 2010 and accumulated CDF luminosity (~ 5 fb^{-1} in 2008) is already tens times that of Run I. A higher collision energy $\sqrt{s} = 1.96$ TeV and improved acceptance of the upgraded detector should further increase the Run II top-quark yield. This allows making more precise studies of the top-quark properties.

The masses of quarks are not predicted by theory, and therefore represent free parameters in the Standard Model (SM) and must be measured experimentally. Tevatron Run I yielded for the top-quark mass of (178.0 ± 4.3) GeV/c^2 [2] that is approximately 40 times heavier than the bottom quark. Investigation of the top quark could help in understanding the mechanism of electroweak symmetry breaking [3], since its mass is close to the vacuum expectation value of as yet unobserved Higgs boson [4]. It is known that the most preferable framework for description of electroweak symmetry breaking is Higgs mechanism.

The masses of Higgs and top quark are coupled with W-boson mass through radiative corrections. The large contribution to quark-loop corrections of electroweak parameters from the heavy top quark provides for powerful tests of the Standard Model (SM). From this point of view, a precise measurement of the top-quark mass is a very important task. At the Tevatron, in the Run II $p\bar{p}$ collisions with a center-of-mass energy of 1.96 TeV, top quarks are produced mainly in $t\bar{t}$ pairs, through $q\bar{q}$ annihilation ($\approx 85\%$) and gluon–gluon fusion. As long as its large decay width and consequently short lifetime ($\sim 10^{-25}$ s), the top quark decays before any hadronization, so that its existence as a «free quark» (first time in «quark lives») can be studied without the complication of lower energy QCD effects. In the framework of SM, each top quark decays mainly to a W boson and a bottom quark. The b quark hadronizes into a jet of particles, while W decays either to a $q\bar{q}$ or to a lepton–neutrino pair. The «all hadronic» mode, where both Ws decay into $q\bar{q}$ pairs, occurs for $\sim 44\%$ of $t\bar{t}$ events; this topology is dominated by a large QCD multijet background. The most precise top-quark mass measurements currently arise from the «lepton + jets» mode ($\approx 30\%$ of events, without tau-leptons), $b\,\ell\,\nu_\ell\,\bar{b}\,q\,\bar{q}'$, where only one W decays hadronically, while

the other decays into lepton mode either with an electron or with muon plus a neutrino, whose presence can be revealed from missing energy in the detector. A third mode occurs when both W bosons from each top quark decay into leptons: $t\bar{t} \rightarrow \bar{b}\,\ell^{-}\bar{\nu}_{\ell}\,b\,\ell'^{+}\nu'_{\ell}$. This, so-called «dilepton» mode, accounts for only $\sim 5\%$ $t\bar{t}$ events (not counting tau-lepton decays). Dilepton events measurements are also important as they allow one to reduce the overall uncertainty on the top-quark mass. Besides, these measurements test the consistency of top-quark mass results obtained by measurements of other W-decay modes, as the dilepton mode contains different and less background sources and represents a different event sample. Since all top-quark mass measurements assume a sample composition of $t\bar{t}$ and Standard Model background events, any discrepancy among the measured top masses taking place from identical $t\bar{t}$ collisions could indicate the presence of new physics out of SM.

There are several top-quark mass reconstruction methods developed for each of the mentioned decay modes. The methods could be subdivided into two main classes: 1) template methods, and 2) Matrix Element Technique methods. The CDF/JINR group measured the top-quark mass using the template methods both in $\ell+$ jets and dilepton channels of top-quark decay [5–7]. The top-quark mass obtained in $\ell+$ jets mode [8], with the CDF/JINR group participation, is one of the most precise current single measurements on this important physical parameter. Recent top-quark mass measurement in dilepton channel in 2.1 fb^{-1} used lepton + isolated track (with neutrino φ weighting) event selection to collect more events due to relaxed cuts for one of leptons.

The previous review made in this periodical by the CDF/JINR group [9], accented mainly on the so-called «Template Method», where briefly was considered «Dynamical Likelihood Method» (DLM) [10].

In this review top-quark mass measurement using Matrix Element Method for dilepton and lepton + jets decay modes will be considered. As it stands now, the most precise measurements of the top-quark mass are obtained with this kind of technique.

The first observation of B_S oscillations — very interesting new phenomena — will be described afterwards. In the end, we talk about new observed objects: heavy baryons, with inclusive heavy b quark.

1. DETECTOR AND EVENT SELECTION

1.1. Detector. The Collider Detector at Fermilab (CDF) is a general-purpose detector observing $p\bar{p}$ collisions at Fermilab's Tevatron. The detector geometry is cylindrical with forward–backward symmetry. The coordinate system has its origin at the center of the detector with the z-axis pointing in parallel to the proton beam direction. The coordinates x, y, r, and φ are defined in the transverse
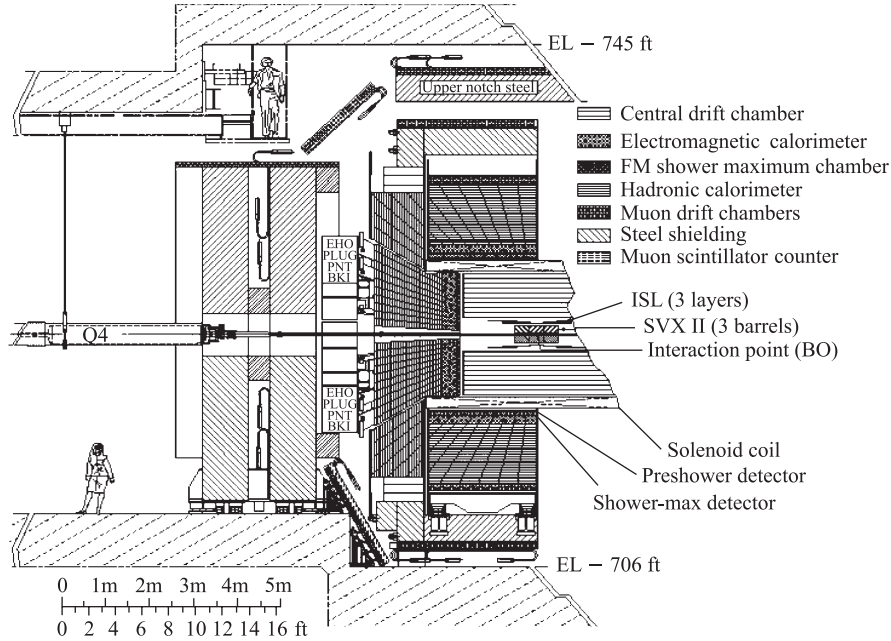
Fig. 1. CDF side elevation view

plane, with the x-axis pointing outward from the accelerator ring, and the y-axis pointing straight up. The angle θ is the polar angle measured from the proton direction, and $\eta = -\ln(\tan(\theta/2))$ is the pseudorapidity. Transverse quantities of energy and momentum, $^*E_T$ and p_T, are magnitudes of projections into the plane perpendicular to the z-axis. Figure 1 shows an elevation view of the CDF detector. The relevant subdetectors are described briefly below. A more complete description of the CDF Run II detector is provided elsewhere [11]. However, here we would like to mention only one point: a separate control of the beam luminosity in the $3.7 < |\eta| < 4.7$ local region that can be done by gas Cherenkov counters that measure the average number of inelastic $p\bar{p}$ collisions per crossing bunch.

The CDF tracking system is the first detector element crossed by a particle leaving the interaction point in the central region. The silicon detectors [12] provide three-dimensional position measurements with very good resolution for charged particles close to the interaction region, allowing extrapolation of tracks back to the collision point and reconstruction of secondary, displaced vertices.

There are a total of 722,432 channels that have a typical strip pitch of 55–65 μm for axial strips, 60–75 μm for $1.2°$ small-angle stereo strips, and

125–145 μm for 90° stereo strips. The silicon detector is divided into three separate subdetectors. The layer 00 (L00) is a single-sided layer of silicon mounted directly on the beam pipe (made of beryllium), at a radius of 1.4–1.6 cm, providing an axial measurement close to the collision point. The SVX II detector is 90 cm long, $|\eta| < 2$, it contains 12 wedges in φ, each with 5 layers of silicon at radii from 2.5 to 10.6 cm. One side of each layer contains strips oriented in the axial direction, and the other side contains 90° stereo strips in three cases, and 1.2° small-angle stereo strips in two cases. The Intermediate Silicon Layers (ISL) comprise three additional layers of double-sided silicon at larger radii: at 22 cm for $|\eta| < 1$, and at 20 and 28 cm for $1 < |\eta| < 2$. Each layer of the ISL provides axial and small-angle stereo measurements.

The Central Outer Tracker (COT) [13] measures particle locations over a large radial distance, providing precise measurements of track curvature up to about $|\eta| = 1$. It is a large open-cell drift chamber with 8 «superlayers» (4 axial and 4 with a 2° stereo angle), each of which contains 12 wire layers, for a total of 96 layers. There are 30,240 wires in total. The COT active volume is 310 cm in length and covers from 43 to 132 cm in radius. An axial magnetic field of 1.4 T is provided by a superconducting solenoid surrounding the silicon detectors and central drift chamber.

Sampling calorimeters measure particle energies. The calorimeters are segmented into towers with projective geometry. The segmentation of the CDF calorimeters is rather coarse, so that often several particles contribute to the energy measured in one tower. In the central region, i.e., $|\eta| < 1.1$, the calorimeter is divided into wedges subtending 15° in φ. Each wedge has ten towers of roughly equal size in η on each side of $\eta = 0$.

The Central Electromagnetic Calorimeter (CEM) [14] contains alternating layers of lead and scintillator, making 18 radiation lengths of material, $0 < |\eta| < 1.28$. The transverse energy resolution for high-energy electrons and photons is $\sigma(E_T)/E_T = 13.5\%/\sqrt{E_T[\text{ GeV}]} \oplus 2\%$. Embedded in the CEM is a Shower Maximum Detector (CES). The CES provides good position measurements of electromagnetic showers at a depth of six radiation lengths and is used in electron identification. The CES consists of wire proportional chambers with wires and cathode strips providing stereo position information. In front of CES is located Preshower Detector, CPR2, which replaced the old slow drift chambers and at present is a completely new construction [15], made from 2800 scintillation tiles contributed by Dubna group. The tile light yield gives up to 36 photoelectrons and guarantees a high γ-pointing accuracy and precision of energy reconstruction essential for c, b, t studies. It also improves electron–meson separation. The tile scintillators were produced in Kharkov and at the Dzhelepov Laboratory of Nuclear Problems, JINR.

The Central Hadronic Calorimeter (CHA), $0 < |\eta| < 1.28$, and the End Wall Hadronic Calorimeter (WHA) [16] are of similar construction, with alternating

layers of steel and scintillator (4.7 interaction lengths). The WHA fills a gap in the projective geometry between the CHA and the end plug calorimeter.

The calorimetry [17] in the end plugs ($1 < |\eta| < 3.6$) has a very complicated tower geometry, but a 15° wedge pattern is respected. The Plug Electromagnetic Calorimeter (PEM) has lead absorber and scintillating tile read-out with wavelength shifting fibers. An electron traversing the PEM passes through 23.2 radiation lengths of material. The energy resolution for high-energy electrons and photons is $\sigma(E)/E = 14.4\%/\sqrt{E \text{ [GeV]}} \oplus 0.7\%$. There is a Shower Maximum Detector (PES), whose scintillating strips measure the position of electron and photon showers.

The Plug Hadronic Calorimeter (PHA) has alternating layers of iron and scintillating tile, for a total of 6.8 interaction lengths. Muon identification is performed by banks of single-wire drift cells four layers deep. The central (CMU) [18] (drift chamber) is located directly behind the hadronic calorimeter in a limited portion of the central region ($|\eta| < 0.6$). The Central Muon Upgrade (CMP) (drift chamber) adds additional coverage in the central region and reduces background with an additional 60 cm of steel shielding, corresponding to 2.4 interaction lengths at 90°. The Central Muon Extension (CMX) (drift chamber) covers the region $0.6 < |\eta| < 1.0$, and contains eight layers of drift tubes, with the average muon passing through six.
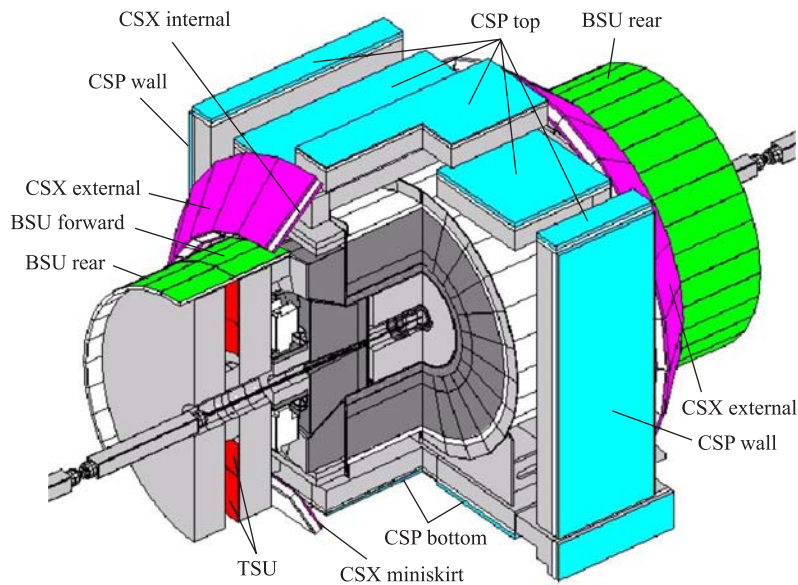

Fig. 2. CDF II muon scintillator system

The CDF/JINR group played a key role in upgrade of CDF muon complex (Fig. 2) to adjust detector to a new luminosity level $2 \cdot 10^{32}$ cm$^{-2} \cdot$ s^{-1} [19]. There are about 1200 muon scintillation counters in the CDF II detector. About 600 of them are the new-type high efficiency counters (made by JINR). On the whole, JINR counters reach 60% of scintillator cover. The longest, up to 320 cm, of the counters cover central region, $|\eta| < 0.6$, and are known as Central Scintillator Upgrade (CSP) counters [19]. All these counters were added to the muon trigger. The old CSP wall deteriorated counters were revived, but still should be replaced by new ones. The Dubna group will do this job soon. The 272 units of CSX conical hodoscope were fully revived and included to Level 1 trigger. The CSX azimuthal coverage was also completed by new addition of two 90° sectors. To extend the muon coverage up to $|\eta| = 1.5$ two overlapping barrel hodoscopes of 160 cm scintillators (450 units BSU) that cover barrel drift chambers were designed and constructed in Dubna. The scintillators used are a polystyrene-based plastic developed by the Institute for Single Crystals of NAS of the Ukraine (Kharkov), under JINR supervision [20, 21].

Monitoring and Control system of muon scintillation counters is the CDF/JINR responsibility. The system [22] comprises the «old» scintillation counters, which were used in Run I (CSX, Miniskirts and CSP wall) and new counters manufactured for Run II (BSU, TSU, CSP, see Fig. 2). The hardware system for the «old» counters is based on the old voltage distributors (Pisaboxes), driven by CAMAC electronics. A PC through interfaces controls the hardware. The new counters are controlled by fast Control and Concentrator Units (CCU). Each CCU supervises the operation of up to 48 counters. Only the manual high-voltage control was available for counters before Run II. It was very obsolete system. Moreover, it did not allow checking counter conditions. The counter voltages were checked manually only few times per year and, as a result, at least 10% of counters actually did not work during quite a long time (some weeks or even months).

Therefore, Dubna group has proposed to create programs for automatic control of high voltage of all muon scintillation counters. As a result of those efforts, JINR group created an efficient modern slow control complex for muon counters at CDF for the first time. There was created database that contains the full information about all counters and system of programs, which compares this database with real values. If the real data do not correspond to real data for one or more counters, error occurs with detailed information on what has happened to counter photomultipliers. Now this program is integrated to the global CDF Monitoring Control System with the embedded instructions for shift crew.

1.2. Trigger. In the present Tevatron data taking period at $\sqrt{s} = 1.96$ TeV, the bunch-crossing interval is 396 ns and peak luminosity is climbing toward of $> 3 \cdot 10^{32}$ cm$^{-2} \cdot$ s^{-1}. The challenge for hadron collider experiments is an extraction signal of interest efficiently from much larger background. To illustrate the

order of magnitude, let us compare the total inelastic cross section at Tevatron energy, ~ 50 mb, with the b-quark production cross section within CDF acceptance ($p_T > 6$ GeV, rapidity $|y| < 1$) that is about 10 μb, and t-quark production cross section 6 pb. It is important also that at luminosity above $0.35 \cdot 10^{32}$ cm$^{-2} \cdot$ s^{-1}, the mean number of interaction per beam crossing exceeds 1. As a whole, this implies that at DAQ output rate ~ 70 Hz trigger rejection should be $\geqslant 25000$.

The CDF uses a three-level trigger. On each beam crossing (396 or 132 ns), the entire front-end digitizes all detectors information. A 5.5 μs pipeline of programmable logic forms axial drift chamber tracks and can match these with calorimeter and muon-chamber data. At Level 1 accept, front-end boards store the event to one of four buffers. Level 2 processing, with about 30 μs latency, adds fast silicon tracking, calorimeter clustering, and EM calorimeter shower-max data. The final Level 2 decision is made in software on a single-board computer, so a wider range of thresholds and derived quantities is possible (e.g., transverse mass of muon track pairs), even for information that is in principle available at Level 1. At Level 2 accept, front-end VME crates transmit to the event builder. At Level 3, a farm of 250 commodity PCs runs full event reconstruction. This is the first stage at which three-dimensional tracks (e.g., for invariant mass calculation) are available. Events passing Level 3 are written to disk.

The further analysis depends on the physical task. For purpose of this review we use data from triggers based on high-p_T leptons, which come from the leptonically decaying W in the event. The first two trigger levels perform limited reconstruction using dedicated hardware, including the eXtremely Fast Tracker (XFT), which reconstructs tracks from the COT in the $r - \varphi$ plane with a momentum resolution better than 2% p_T (GeV/c) [23]. The electron trigger requires a coincidence of an XFT track with an electromagnetic cluster in the central calorimeter, while the muon trigger requires that an XFT track points toward a set of hits in the muon chambers. To extract b quark and its decay products at Level 2, SVT system is used (see below). The third level is a software trigger that performs full event reconstruction. Electron and muon triggers at the third level require fully reconstructed objects as in the event selections described below, but with looser criteria.

Many of CDF physics triggers [19] used muon detectors. The corresponding geometrical coverage of pseudorapidity $|\eta|$ is shown in Fig. 3.

As an example, let us consider muon trigger for the IMU zone.

The IMU trigger of the first level (L1) «geometrically» covers the front ($1.0 \leqslant |\eta| \leqslant 1.25$) and rear ($1.25 \leqslant |\eta| \leqslant 1.5$) muon detectors comprising the IMU subsystem (Fig. 3). In the range $1.0 \leqslant |\eta| \leqslant 1.25$, the muon trigger is formed by the coincidence of signals from the BSU$_F$ counters and the BMU drift chambers, the track-extrapolation system (XTRP). After a track in the Central Outer Tracker (COT) is identified by the eXtremely Fast Tracker (XFT), it is extrapolated to the BMU chambers by the XTRP (Fig. 3).
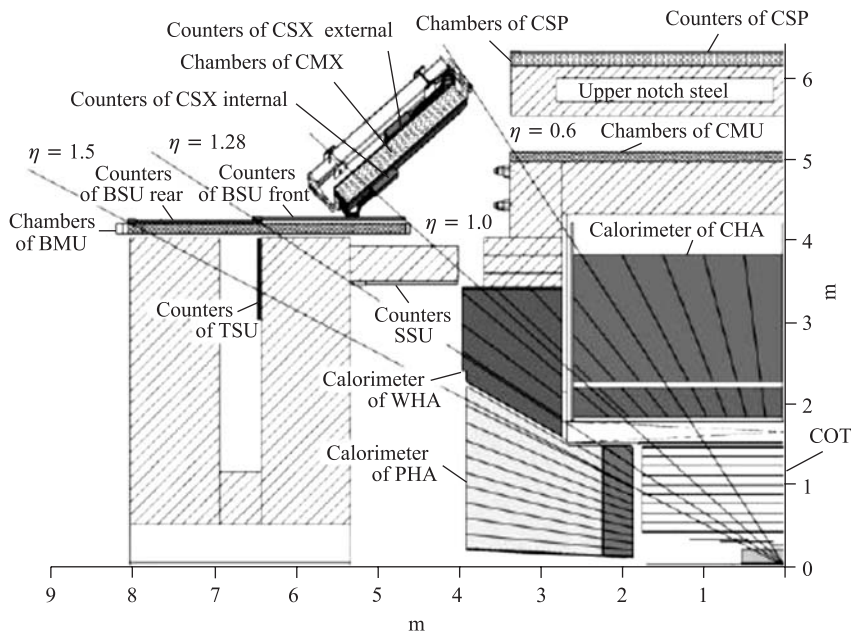
Fig. 3. $|\eta|$ zones of muon and other detectors that can be switched in triggers

Signals (the information from towers of the WHA hadron calorimeter with corresponding η (Fig. 3) of the hadron timing system (HTS)) are used in the trigger for synchronization with muons originating in the collision area [19].

In the region $1.25 \leqslant |\eta| \leqslant 1.5$, the muon trigger is formed by the coincidence of signals from counters of BSU_R and TSU, the BMU drift chambers, and the hadron timing system. Signals (the information from towers of the WHA and PHA hadron calorimeters with corresponding η (Fig. 3) of the hadron timing system (HTS)) are used in the trigger for synchronization with muons produced in the collision area.

The logic of the IMU trigger L1 is built as follows [24]:

(i) L1F = BSU_F & BMU & XTPR & WHA for the forward part, and

(ii) L1R = BSU_R & TSU & BMU &(WHA + PHA) for the rear part.

These triggers are included as a part of more complicate common triggers.

At an initial instant luminosity of $1.2 \cdot 10^{32}$ cm$^{-2} \cdot$ s^{-1}, the rate of the L1 trigger did not exceed 200 and 300 Hz, respectively, for the forward and rear parts of the IMU system (October 2005). For large luminosity this trigger condition is used as part of an off-line treatment.

Depending on the investigation task, additional requirements are imposed upon the trigger of the second level.
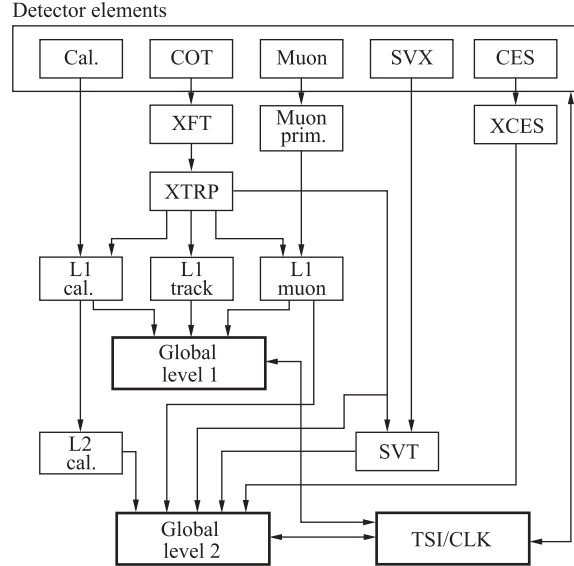
Detector elements

Fig. 4. Diagram of common Level 2 trigger

Block diagram for common trigger of Level 2 is shown in Fig. 4. The abbreviations used here are already mentioned above with the exception of TSI/CLK and SVT. TSI/CLK corresponds to Clock in electronics and Detector firmware and SVT signifies Silicon Vertex Trigger that will be described below. The SVT was created with strong contribution by CDF/JINR group participation to study c, b physics.

1.3. SVT System. SVT is new processor for reconstruction of charged particles at Level 2 of the trigger [25]. It takes 20 μs to make a decision. That means for SVT working in parallel for making different tasks such as reconstruction of hit coordinates, fit track roads, fitting track parameters with large accuracy.

The physical reason for introducing additional processing operations of the SVT [25, 26] is the essential necessity to pick out vertices of B-meson decays by finding tracks with large impact parameters. At CDF conditions B mesons have a range path ~ 500 μm and impact parameters of the product tracks are about 100 μm. Detection of secondary vertex at trigger level allows decreasing $p\bar{p}$ inclusive background by a factor of about 1000 because of ratio corresponding cross sections. This allows one to pick up events of $B \to \pi\pi$ and $B_s \to D_s\pi$, which are very interesting in different aspects (CP violation, B_s oscillation).

The Silicon Vertex Trigger (SVT) is a system of 150 custom VME boards that reconstructs transverse track projections in the CDF silicon strip detector in

15 μs delay. SVT's impact parameter resolution (~ 30 μm) enables Level 2 trigger (Fig. 4) to distinguish primary and secondary particles of an interaction, and hence to collect large samples of hadronic bottom and charm decays.

The SVT refines the Level 1 tracking information from the eXtremely Fast Tracker (XFT), which reconstructs tracks in the Central Outer Tracker (COT), by linking Silicon Vertex Detector (SVX II) hits. Track reconstruction is performed by SVT in the plane transverse to the beamline. The Level 2 latent time is about 20 μs, therefore the design of the SVT has been concentrated on performing the various tasks in parallel: hits reconstruction from the single-strip pulse height, pattern recognition and final high precision track fitting.

The core of the SVT is organized as 12 identical systems (sectors) running in parallel independently. This architecture derives from the geometry of the SVX II detector, which is divided into 12 identical wedges along the azimuthal angle. The SVX II is also segmented into 6 half barrels along the beamline.

The main functional blocks of each SVT sector are the Hit Finders, the Associative Memory system, the Hit Buffer and the Track Fitter (Fig. 5).

Every time the Level 1 trigger accepts an event, the digitized pulse heights in the Silicon Vertex Detector are sent to the Hit Finders, which calculate hit positions. The hits found by the Hit Finders and the tracks found in the COT are then fed simultaneously to the Associative Memory system and to the Hit Buffer. The Associative Memory system performs pattern recognition by selecting for further processing only combinations of COT tracks and SVX II hits which represent good track candidates.

The list of Roads found by the Associative Memory system is sent to the Hit Buffer, which retrieves the original full-resolution silicon hit coordinates and the XFT track associated with each Road and delivers them to the Track Fitter. The Track Fitters check all the hit combinations in each Road and calculate the track parameters with full detector precision.
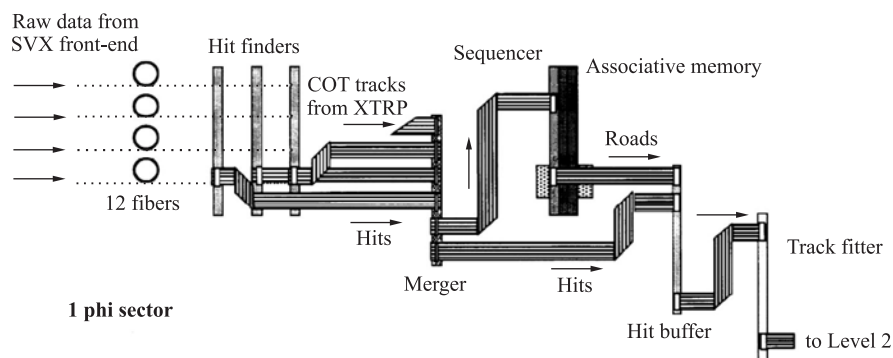

Fig. 5. SVT hardware implementation

The Silicon Vertex Trigger has been commissioned and operated successfully for CDF Run II physics data [27–34]. Among the key reasons for this system's success are its modular architecture and its ability to sink and source test data at a wide range of pipeline stages, both in tests and during beam runs.

The JINR contribution to SVT project covers different key stages:

• Simulation of the pattern recognition.

• Simulation of the SVT timing and resolution. There was estimated the SVT operation time for the forthcoming Run II. The SVT operation time for most of events from $B^0 \to \pi^+\pi^-$ decays in Run II will be in range between 8.6 and 10.8 μs. Obtained SVT impact parameter resolution is 31.3 μm.

• Preparation by simulation track image libraries for Associative Memory board (AM) and its testing.

• Processing of the SVT data: real-time track reconstruction using information from the Silicon Vertex Detector.

• Off-line and on-line SVT monitoring. Very effective off-line monitoring system was created: it monitors main parameters of the SVT daily (job luminosity, D^0 cross section, beam position table, table of trigger paths used for SVT efficiency calculation, average SVT efficiency, number of SVT failures obtained from SVTSIM comparison). The system starts and works automatically, producing Ntuples (equivalent DST) for every Run. The SVT group members widely use all this information. The On-line SVTD monitor module shows status SVT information on common slide for Consumer Operator.

Described above CDF set-up is being used in Run II that started in 2001. It accumulated an integrated luminosity, which exceeds the luminosity of the first Run by approximately 50 times. Increased energy of the Tevatron and acceptance of set-up also helped to enlarge the number of events under study. All this improves situation for investigations of very rare phenomenon such as top-quark production.

The next part is devoted just to this subject.

2. TOP QUARK STUDY

As we have mentioned in Introduction there are 3 main top-quark decay modes, which are under study in experiments at the Tevatron: «All hadronics», «lepton + jets» and «dilepton» in accordance with W decay modes. Each of these modes is subdivided into groups depending on a method of treatment of raw event samples. There is no sense in description of all these methods in the review, much better is to send readers to the original articles. Besides, one can look in the previous review published in this periodical [9], where «lepton + jets» with «Dynamical Likelihood Method» (DLM) [10] and «dilepton» modes with the «template» method evaluation of the results are considered.

In this part we consider other cases: «dilepton» and «lepton + jets» decays using Matrix Element Method. But first of all, let us have a look at what happened at the very beginning.

Top quark was observed for the first time in 1995. And here is the press release devoted to this historical event [1]: *«Discovery of the Top Quark* (from Chris Quigg, Fermi National Accelerator Laboratory). Ever since the existence of the bottom (or b) quark was inferred from the discovery of the upsilon family of resonances at Fermilab in 1977, particle physicists have been on the lookout for its partner, called top (or t).

The long search, which occupied experimenters at laboratories around the world, came to a successful conclusion in February 1995 with the announcement that the top (or t) quark had been observed in two experiments at the Tevatron proton–antiproton collider at Fermilab [1].

Top is the last of the fundamental constituents of subnuclear matter that theories of the strong, weak, and electromagnetic interactions and a wealth of experimental information had led particle physicists to expect. Theoretically, the top's existence was required to make the electroweak theory internally consistent. Experimentally, the top's existence was signaled by the pattern of disintegrations of the b quark and, by the way, b quarks interacted with other particles via the exchange of Z bosons. A year before the formal discovery, a growing body of observations pointed to the existence of a top quark with a mass of about 180 GeV/c^2 ((PDG — Particle Data Group // Phys. Rev. D. 1994. V. 50, No. 3) data pointed to top mass $\left(174 \pm 10^{+13}_{-12}\right)$ GeV/c^2, measured by CDF in $p\bar{p}$ collision). Finding top there emerged as a critical test of the understanding built up over two decades.

Creating top–antitop pairs in sufficient numbers to claim discovery demanded exceptional performance from the Tevatron, at 1.8 TeV the world's highest-energy collider. Observing traces of the disintegration of top into a b quark and a W boson required highly capable detectors and extraordinary attention to experimental detail. Both the b and the W are themselves unstable, with many complex decay modes.

Both groups (CDF and D∅) found events in which one or both Ws decayed into an electron or muon, plus a neutrino. A significant number of these events showed evidence for one or two b quarks as well. Taken together, the populations and characteristics of different event classes provided irresistible evidence for a top quark with a mass in the anticipated region: $(178 \pm 8 \pm 10)$ GeV/c^2 for CDF (the first uncertainty refers to that due to the statistical size of the data sample, while the second refers to that due to systematic uncertainties, which include imperfect knowledge of the detectors, theoretical modeling, and algorithms for estimating the mass); and $(199 \pm 20 \pm 22)$ GeV/c^2 for D∅. Meanwhile, the top–antitop production rate was in line with theoretical predictions.

Top is a most remarkable particle, even for a quark. Although a single top quark weighs about as much as an atom of gold, we expect that it is structureless down to a scale of at least 10^{-18} m. Its expected lifetime of about $0.4 \cdot 10^{-24}$ s makes it by far the most ephemeral of the quarks, and opens new possibilities for the study of quark dynamics.

Because of the great mass and short lifetime, it is popular to say that top quarks were produced in great numbers in the fiery cauldron of the Big Bang, that they disintegrated in the merest fraction of a second, and then vanished from the scene until physicists learned to create them at the Tevatron. To learn how it helped sow the seeds for the primordial universe that evolved into our world of great complexity and change, it would be reasonable enough to care about the top. But this cosmic role is not the whole story; it invests the top quark with a remoteness that veils its importance for the everyday world of today. The real wonder is that here and now, every minute of every day, the top quark affects the world around us.

For example, by virtue of the Heisenberg uncertainty principle, top quarks and antiquarks wink in and out of an ephemeral presence in our world. Though they appear virtually, fleetingly, on borrowed time, top quarks have real effects of immediate interest to particle physicists that is the influence of top on the mass of the W boson, which regulates the rate of radioactive decay and the rate of energy production in the Sun. Rapidly improving measurements of both the top mass and the W mass set the stage for another incisive test of the electroweak theory.

The Standard Model suggests that the electroweak force separated into the separate electromagnetic and weak forces in the early Universe, and that the Higgs boson bestowed a great mass on the W and Z bosons, the carriers of the weak force, while allowing the photon, the carrier of the electromagnetic force, to remain massless.

But what is the mass of the Higgs itself? Because the W mass is fine-tuned by the influence of the Higgs boson, particle physicists hope that better estimates of the top mass and the W mass will narrow the range of possible masses for the Higgs boson.

Like the end of many a scientific quest, the discovery of top marks a new opening. The first priority, with the doubled event samples that will be in hand by the end of 1995, is to refine the measurements of the top mass. It is already possible to begin asking how precisely the top conforms to prior expectations as to its production and decay rates. Also, because of top's great mass, its decay products may include unpredicted or at least undiscovered new particles. A very interesting development would be the observation of resonances in top–antitop production that would give new clues about the breaking of electroweak symmetry.

For the moment, the direct study of the top quark belongs to the Tevatron. Furthermore, the Large Hadron Collider at CERN will produce tops at more than 10,000 times the rate seen in the original discovery experiments. Also, electron linear colliders may add new opportunities for the study of top-quark properties and dynamics.

In the meantime, the network of understanding of elementary particle interactions known as the Standard Model links the properties of top quarks to a variety of phenomena to be explored in other experiments. (From APS News-Online/Physics News in 1995 (May 1996) Copyright 1996, the American Physical Society.)»

2.1. Precision Measurement of the Top-Quark Mass from Dilepton Events Using Matrix Element [35]. The dilepton channel, including decays with two charged leptons in the final state $t\bar{t} \to W^+ b W^- \bar{b} \to b' \ell'^+ \nu_{\ell'} \bar{b} \ell^- \bar{\nu}_\ell$, has a small branching fraction ($\sim 5\%$) but has the fewest jets in the final state, giving a smaller dependence on the calibration of the jet-energy scale and less ambiguity in jet-quark assignments. Discrepancies between measurement results in different decay channels could indicate contributions from physics beyond the Standard Model [36].

The feature of the dilepton channel is that two neutrinos from W decays escape undetected and this is a unique challenge in reconstructing of events. Measurements of M_t in this channel made using Run I data [38, 39] and recent measurements made using Run II data [44] utilize methods that make a series of kinematics assumptions. The greatest statistical precision, however, was achieved through the application of a Matrix Element Method [41,45,46] which makes minimal kinematic assumptions; instead integrating the leading-order matrix element for $t\bar{t}$ production and decay over all unconstrained quantities. The first application of this method to the dilepton channel by the CDF collaboration [37, 47] used 340 pb^{-1} of Run II data.

Here we describe an analysis, which used an enhanced version [48] of the Matrix Element Method presented in [47]. The enhanced method accounts for initial-state radiation from the incoming partons and has substantially improved statistical power. This measurement uses data collected by the CDF II detector between March 2002 and March 2006 corresponding to an integrated luminosity of 1.0 fb^{-1} and includes 340 pb^{-1} used in [47].

The trigger requires, as in [47], at least one high-p_T lepton. For central electron candidates, the first two trigger levels require an electromagnetic calorimeter cluster with a confirming COT track and without a large hadronic energy deposit. The third-level trigger requires an electron candidate with $E_T \geqslant 18$ GeV. Events with electron candidates in the plug ($|\eta| > 1.2$) are required to have electron $E_T > 20$ GeV and missing transverse energy $\not{E}_T > 15$ GeV. (Missing transverse energy, $\not{E}_T$, is defined as the magnitude of the vector, $- \Sigma i E_T^i \mathbf{n}_i$, where E_T^i are the magnitudes of transverse energy contained in each calorimeter tower i,

and $\mathbf{n}_i$ is the unit vector from the interaction vertex to the tower in the transverse (x, y) plane.) For muon candidates, the first two trigger levels require hits in the muon chambers and a confirming COT track. The third-level trigger requires a muon with a matching track of $p_T \geqslant 18$ GeV/c. Two oppositely charged leptons with $E_T > 20$ GeV are required. One lepton, the «tight» lepton, must pass strict lepton identification requirements and be isolated. A lepton is isolated if the lepton total E_T, within a cone $\Delta R \equiv \sqrt{(\Delta\eta)^2 + (\Delta\varphi)^2} \leqslant 0.4$, is $> 90\%$ of the total E_T in the cone ΔR. Tight electrons have a well-measured track pointing at an energy deposition in the calorimeter. For electrons with $|\eta| > 1.2$, this track association uses a calorimeter-seeded silicon tracking algorithm [44]. In addition, the candidate's electromagnetic shower profile must be consistent with that expected for electrons. Tight muons must have a well-measured track linked to hits in the muon chambers and energy deposition in the calorimeters consistent with that expected for muons.

The other lepton, the «loose» lepton, is required to be an electron or muon selected as above, with the exceptions that it need not be isolated and muon identification requirements are relaxed. These selections add acceptance for dilepton events where electrons or muons pass through gaps in the calorimetry or muon systems. They also contribute acceptance for single prong hadronic decays of the τ lepton from $W \to \tau\nu$ (12%).

Candidate events must have $\not\!\!E_T > 25$ GeV. To reduce the occurrence of false $\not\!\!E_T$ due to mismeasured jets, there is a requirement that the $\not\!\!E_T$ vector point away from any jet. To further suppress false $\not\!\!E_T$ arising from mismeasurement of their respective loose leptons, it is required that the $\not\!\!E_T$ vector be at least $20°$ from the closest lepton.

Analysis counts jets with $E_T > 15$ (20) GeV detected in $|\eta| < 2.5$ (2.0), where a jet is defined as a fixed-cone cluster with a cone size of $R = 0.4$. The jet E_T measurements are corrected for the effects of calorimeter nonuniformity and absolute energy scale [45].

Authors applied also removal cosmic muons and photon-conversion electrons. These selection cuts yield 78 candidate events. The residual background is considered later.

Analysis Overview. The probability density for $t\bar{t}$ decays is expressed as $P_S(x|M_t)$, where M_t is the pole top-quark mass and x represents the lepton energy, jet energy, and $\not\!\!E_T$ measurements. The $P_S(x|M_t)$ is calculated using the theoretical description of the $t\bar{t}$ production and decay process with respect to x; $P_S(x|M_t)$ is proportional to the differential cross section, $d\sigma(M_t)/dx$:

$$P_S(x|M_t) = \frac{1}{\sigma(M_t)} \frac{d\sigma(M_t)}{dx}, \tag{1}$$

where $d\sigma/dx$ is the differential cross section evaluated with respect to event measurements containing x. To evaluate the differential cross section $d\sigma/dx$,

there was made a convolution of the leading order matrix element M for $q\bar{q} \to t\bar{t} \to bl\nu_l \bar{b}l'\nu_{l'}$ with detector resolution functions and then integration over unmeasured quantities, such as neutrino momenta and quark energies. While quark energies cannot be directly measured, they can be estimated from measured jet energies. The integration over quark energies used a parameterized transfer function $W_{\text{jet}}(p, j)$, which is the probability of measuring jet energy j, given quark energy p. As in [46], authors of [47] assume that lepton energies and quark angles are perfectly measured, that incoming partons are massless and have no transverse momentum, and that the two highest energy jets in the event correspond to the b quarks from $t\bar{t}$ decay. Unlike in [46], authors of [47] do not assume zero transverse momentum of the $t\bar{t}$ system, $p_T^{t\bar{t}}$, which would require no initial-state radiation. Instead, it is inferred likely values of $p_T^{t\bar{t}}$ from unclustered transverse energy. (The unclustered transverse energy in an event is the total transverse energy in the event that is measured in the calorimeter but not clustered into a lepton or jet.) $p_T^{t\bar{t}}$ also includes jets that are not the most energetic in the event. The parameterization takes place as the relation between these measured quantities and $p_T^{t\bar{t}}$ as a transfer function, $Wp_T(p_T^{t\bar{t}}, U)$, where U is a sum of the unclustered transverse energy and subleading jet transverse energies in an event. Both $W_{\text{jet}}(p, j)$ and $Wp_T(p_T^{t\bar{t}}, U)$ are estimated using $t\bar{t}$ events generated with HERWIG [50] and the CDF II detector simulation [51]. This description of the initial state radiation improves the expected statistical uncertainty by 10% compared to the technique described in [46].

The effect of the above assumptions on the final measurement is estimated using Monte Carlo simulation. The expression for the probability density at a given mass for a specific event can be written as

$$P_s(x|M_t) = \frac{1}{N} \int d\Phi |M_{t\bar{t}}(q_i, p_i, M_t)|^2 \times$$
$$\times \prod_{k=1,2} W_{\text{jet}}(p_k, j_k) Wp_T(p_T^{t\bar{t}}, U) f_{\text{PDF}}(q_1) f_{\text{PDF}}(q_2), \quad (2)$$

where the integral $d\Phi$ is over the eight remaining unconstrained unmeasured momenta of the initial and final-state particles, q_1 and q_2 are the incoming parton momenta, p_i are the outgoing lepton and quark momenta, $f_{\text{PDF}}(q_i)$ are the parton distribution functions (PDFs) [53] and $M_{t\bar{t}}(q_i, p_i, M_t)$ is the leading-order $t\bar{t}$ production and decay matrix element as defined in [53] for the process $q\bar{q} \to t\bar{t} \to b\,\ell^+\nu_\ell \bar{b}\ell^-\bar{\nu}_{\ell'}$. (While up to 15% of $t\bar{t}$ pairs at the Tevatron are produced by gluon–gluon fusion ($gg \to t\bar{t}$), this term can be excluded from the matrix element with negligible effect on the precision of the measurement.) The term $1/N$ is defined such that the probability density satisfies the normalization condition, $\int dx P_S(x|M_t) = 1$. The probability for both possible jet-parton assignments (1), (2) is evaluated and summed. This sum is expressed as explicit

function of two flavors (a, b) of incoming partons. One example is shown at evaluation of signal probability.

Signal Probability. The probability density for $q\bar{q} \to t\bar{t} \to bl\nu_l\bar{b}l'\nu_{l'}$ decays is constructed as the differential cross section, $d\sigma$, with respect to the measured event quantities, x. The total cross section σ is written as

$$\sigma = \int \sum_{a,b} \frac{(2\pi)^4 |M|^2}{4\sqrt{(q_1 \cdot q_2)^2 - m_1^2 m_2^2}} f_{\mathrm{PDF}}^a \left(\frac{q_{z1}}{E_{\mathrm{beam}}}\right) f_{\mathrm{PDF}}^b \left(\frac{q_{z2}}{E_{\mathrm{beam}}}\right) d\Phi_6 \, dq_1 \, dq_2,$$

(3)

where the sum runs over incoming parton (a, b) flavors, M is the matrix element for the process, $q_{1,2}$ and $m_{1,2}$ refer to the momenta and mass of the incoming partons, f_{PDF} are the parton distribution functions for flavor $a(b)$, and the integration is over the phase space for the six final state particles as well as the longitudinal momenta of the incoming particles.

The matrix element has the form

$$|M|^2 = \frac{g_s^4}{9} F\bar{F}((2 - \beta^2 s_{\mathrm{qt}}^2) - X_{\mathrm{sc}}),$$

where β is the top-quark velocity in the $q\bar{q}$ rest frame, X_{sc} contains terms describing spin correlations between the top quarks, g_s is the strong coupling constant $(g_s^2/4\pi = \alpha_s)$, s_{qt} is the sine of the angle between the incoming parton and the top quark, and F and $\overline{F}$ are the propagators for the top and the anti-top, respectively. The spin correlation term X_{sc} was dropped as it is negligible. Then, the top-quark propagator and decay terms are given by

$$F = \frac{g_w^4}{4} \left[\frac{m_t^2 - m_{l\nu}^2}{(m_t^2 - M_t^2)^2 + (M_t \Gamma_t)^2} \right] \left[\frac{m_t^2(1 - \hat{c}_{lb}^2) + m_{l\nu}^2(1 + \hat{c}_{lb}^2)^2}{(m_{l\nu}^2 - M_W^2)^2 + (M_W \Gamma_W)^2} \right],$$

where m_t is the invariant mass of the t-quark decay products and $\hat{c}_{ij}$ is the cosine of the angle between particles i and j in the W rest frame. The $M_t, \Gamma_t, M_W, \Gamma_W$ are the pole masses and widths of the top quark and W boson, and g_w is the weak coupling constant. The top width, Γ_t, is a function of M_t, M_W and Γ_W as described by the Standard Model. $\bar{F}$ is given by the same expression as for F, replacing the terms or t and its decay products with $\bar{t}$ and its decay products.

While approximately 15% of $t\bar{t}$ pairs in $p\bar{p}$ collisions at $\sqrt{s} = 1.96$ TeV are produced in gluon–gluon fusion ($gg \to t\bar{t}$), studies have shown that this term can be excluded from the matrix element with very little loss of sensitivity to the measurement. A small systematic uncertainty is derived from theoretical uncertainty in the relative gluon fraction.

The cross section as a function of M_t is expressed as a six-dimensional integral and integration is performed numerically using VEGAS algorithm in the GNU Scientific Library.

Table 2. **Expected numbers of signal and background events for a data sample of integrated luminosity of 1.0 fb^{-1}**

Source	Events
Expected $t\bar{t}$ ($M_t = 165$ GeV/c^2)	63.4 ± 1.7
Expected background	26.9 ± 4.8
Drell–Yan ($Z/\gamma^* \to ll$)	13.1 ± 4.4
Misidentified lepton	8.7 ± 1.5
Diboson (*WW/WZ*)	5.1 ± 1.0
Total expected ($M_t = 165$ GeV/c^2)	90.3 ± 5.1
Run II observed	78

Note. The number of expected $t\bar{t}$ is given for $\sigma_{tt} = 9.1$ pb, which corresponds to $M_t = 165$ GeV/c^2. Other backgrounds are negligible; expected signal and background numbers have an additional correlated uncertainty of 6% from uncertainty in the sample luminosity.

Background. In addition to $t\bar{t}$ production, the probability for dominant background processes was calculated. The final event-by-event probability is then

$$P(x|M_t) = P_S(x|M_t)p_s + P_{b1}(x)p_{b1} + P_{b2}(x)p_{b2} \ldots,$$

where p_s and p_{b1} are determined from the expected fractions of signal and background events (see Table 2).

To determine P_{bi} it is necessary numerically to evaluate background matrix elements using algorithms adopted from the generator ALPGEN [54]. There were calculated probabilities for the following background processes: $Z/\gamma^* \to ee$, $\mu\mu$ plus associated jets, $W+ \geqslant 3$ jets where one jet is incorrectly identified as a lepton, and WW plus associated jets. Authors [47] do not calculate probabilities for $Z \to \tau\tau$ or WZ, comprising 11% of the expected background. Studies indicate that the use of the background probabilities improves the expected statistical uncertainty by 10%. The posterior probability for the sample is the product of the event-by-event probabilities. The mean of the posterior probability, $P(M_t)$, is the raw measured mass, M_t^{raw}, and its standard deviation is the raw measured statistical uncertainty, $\Delta M_t^{\mathrm{raw}}$. Both are subject to corrections described below.

To test the method, Monte Carlo experiments for signal and background events were performed. Signal events are generated using HERWIG for top-quark masses ranging from 155 to 195 GeV/c^2. Background events are modeled using observed events in the case of background due to misidentified leptons; ALPGEN-simulated events in the case of $Z/\gamma^* \to ee$, $\mu\mu$, and events simulated with PYTHIA [55] in the case of $Z/\gamma^* \to \tau\tau$, WW, WZ, ZZ.
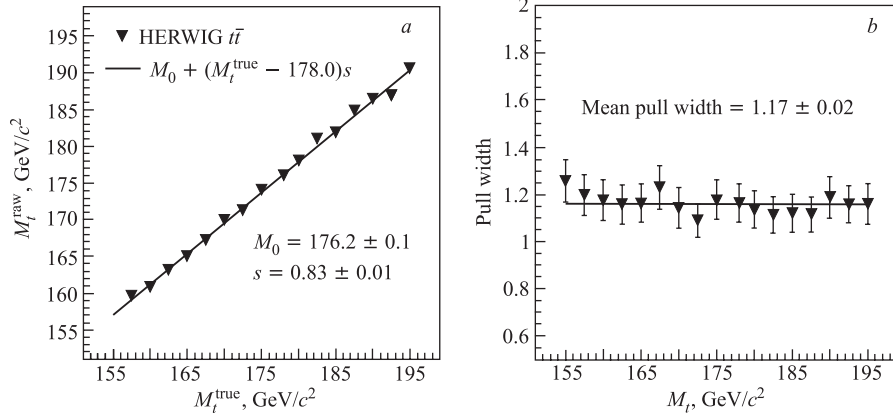
Fig. 6. *a*) Mean measured M_t in Monte Carlo experiments of signal and background events at varying top-quark mass. The solid line is a linear fit to the points. *b*) Pull widths of Monte Carlo experiments of signal and background events at varying top-quark mass. The solid line is the average of all points, 1.17 ± 0.02

The numbers of signal and background events in each Monte Carlo experiment are Poisson-fluctuated values around the mean values given in Table 2. The estimate for the $t\bar{t}$ signal at varying masses is evolved to account for the variation of cross section and acceptance. The response of the method for these Monte Carlo experiments is shown in Fig. 6, *a*. While the response is consistent with a linear dependence on the top-quark mass, its slope is less than unity due to the presence in the sample of background events for which probabilities are not calculated. Corrections, $M_t = 178 \text{ GeV}/c^2 + (M_t^{\text{raw}} - 176.4 \text{ GeV}/c^2)/0.83$ and $\Delta M_t = \Delta M_t^{\text{raw}}/0.83$, are derived from this response and applied to values measured in the data.

The width of the pull distributions in these Monte Carlo experiments, shown in Fig. 6, *b*, where pull is defined as $(M_t - M_t^{\text{true}})/\Delta M_t$, indicates that the statistical uncertainty is underestimated by a factor of 1.17, after applying the corrections described above. These results from the simplifying assumptions described above, made to ensure the computational tractability of the integrals in Eq. (2). The largest effects [46] are the leading two jets in an event not resulting from b-quark hadronization, imperfect lepton momentum resolution, imperfect jet angle resolution, and unmodeled backgrounds. Correcting by this factor of 1.17, authors estimate the mean statistical uncertainty to be 5.0 GeV/c^2 if $M_t = 175 \text{ GeV}/c^2$ or 4.2 GeV/c^2 if $M_t = 165 \text{ GeV}/c^2$.

Applying the method and corrections described above to the 78 candidate events observed in the data, there was measured $M_t = (164.5 \pm 3.9 \text{ (stat.)}) \text{ GeV}/c^2$. Below in Fig. 7 are presented 14 out of 78 of final fit results (in arbitrary units).
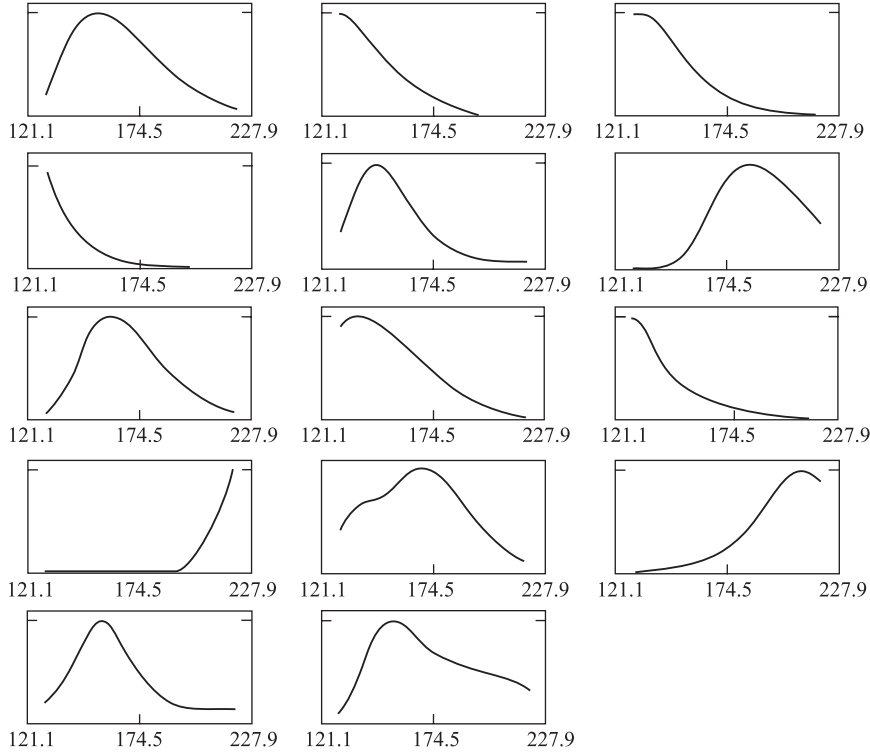
Fig. 7. 14 out of 78 of final fit results (in a. u.)

Figure 8 shows the joint probability density, without systematic uncertainty, for the events in observed data set. The measured statistical uncertainty is consistent with the distribution of statistical uncertainties in Monte Carlo experiments where signal events with $M_t = 165$ GeV/c^2 are chosen according to a Poisson distribution with mean $N_{tt} = 63.4$ events. This number of events corresponds to the cross section and acceptance at $M_t = 165$ GeV/c^2. 31% of these Monte Carlo experiments yielded a statistical uncertainty less than 3.9 GeV/c^2.

A summary of systematic uncertainties in this measurement is shown in Table 3. The largest source of systematic uncertainty in this measurement is due to uncertainty in the jet energy scale [56], which was estimated at 3.5 GeV/c^2 by varying the scale within its uncertainty, including effects of high instantaneous luminosity (which have been found to contribute an uncertainty of 0.2 GeV/c^2). This is necessarily larger than in the previous application of this method [46], as additional jets measurements were included in the calculation; future measurements would benefit from a direct calibration of the b-jet energy scale from
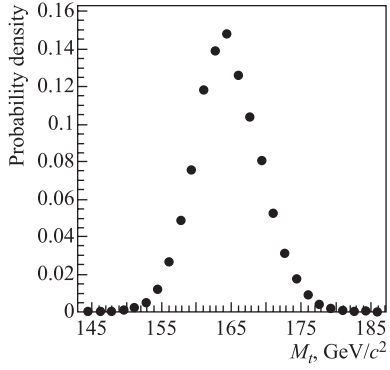
Fig. 8. Joint posterior probability density as a function of top-quark mass for 78 observed candidate events, after all corrections. Systematic uncertainties are not shown

$Z \rightarrow b\bar{b}$ decays. The uncertainty due to the limited number of background available for Monte Carlo experiments is estimated to be 0.7 GeV/c^2. Uncertainties due to PDFs are estimated using different PDF sets (CTEQ5L [52] vs. MRST72 [57]), different values of Λ (QCD) and varying the eigenvectors of the CTEQ6M [52] set; the quadrature sum of these uncertainties is 0.8 GeV/c^2. Uncertainty due to showering model in the Monte Carlo generator used for $t\bar{t}$ events is estimated as the difference in the extracted top-quark mass from PYTHIA events and HERWIG events and amounts to 0.9 GeV/c^2. The uncertainty coming from modeling of the two largest sources of background, Z/γ^* and events with a misidentified lepton, is estimated to be 0.2 GeV/c^2.

Uncertainty due to imperfect modeling of initial-state (ISR) and final-state (FSR) QCD radiation is estimated by varying the amounts of ISR and FSR in simulated events [58], giving 0.3 GeV/c^2 for FSR and 0.3 GeV/c^2 for ISR. The uncertainty in the mass due to uncertainties in the response correction shown in Fig. 5 is 0.6 GeV/c^2. The contribution from uncertainties in background composition is estimated by varying the background estimates from Table 2 within their uncertainties and amounts to 0.7 GeV/c. The uncertainty in the lepton energy scale contributes an uncertainty of 0.1 GeV/c^2 to the measurement. Adding all of

Table 3. **Summary of systematic uncertainties**

Source	ΔM_t, GeV/c^2
Jet energy scale	3.5
Limited background statistics	0.7
PDFs	0.8
Generator	0.9
Background modeling	0.2
FSR modeling	0.3
ISR modeling	0.3
Response correction	0.6
Sample composition uncertainty	0.7
Lepton energy scale	0.1
Total	3.9

these contributions together in quadrature yields a total systematic uncertainty of 3.9 GeV/c^2.

In summary, authors [47] have presented a new measurement of the top-quark mass in the dilepton channel,

$$m_t = (164.5 \pm 3.9(\text{stat.}) \pm 3.9(\text{syst.})) \text{ GeV}/c^2.$$

This is the most precise measurement of m_t in the investigated channel at the date of publication with an approximately 35% improvement in statistical precision over the previous best measurement [46]. The systematic uncertainty, while 15% larger, is nearly completely correlated with systematic uncertainties in measurements in other channels, and so does not impact the global combination, nor an analysis of measurements in different channels. Previous measurements yielded smaller values of m_t in the dilepton channel [37–39] than in the single lepton [40] and all-hadronic [59] decay channels, though the discrepancy was not statistically significant. This measurement continues that trend with substantially increased statistical precision. A global combination [60], however, shows that these variations are consistent with statistical fluctuations.

2.2. Precise Measurement of the Top-Quark Mass in the Lepton + Jets Topology, Using Matrix Element.   Events analyzed in this part represent the single lepton plus jets final states $t\bar{t} \to W^+bW^-\bar{b} \to \ell\nu bq\bar{q}'\bar{b}$. The top-quark mass is extracted using a direct calculation of the probability density that each event corresponds to the $t\bar{t}$ final state. The probability is a function of both the mass of the top quark and the energy scale of the calorimeter jets, which is constrained *in situ* by the hadronic W-boson mass. Using 167 events observed in 955 pb^{-1} of integrated luminosity collected with the CDF II detector from February 2002 to March 2006, there was achieved the most precise single measurement of the top-quark mass $m_t = (170.8 \pm 2.2(\text{stat.}) \pm 1.4(\text{syst.})) \text{ GeV}/c^2$ at the moment of publication [61].

Events in the lepton + jets decay channel are selected to have a single, isolated electron or muon candidate with large transverse energy, large imbalance in transverse momentum in the event (missing transverse energy $\not{E}_T$) as expected from the undetectable neutrino, and exactly four jets with large transverse energy. Jets are reconstructed using a cone algorithm with radius $\Delta R \equiv \sqrt{(\Delta\eta)^2 + (\Delta\varphi)^2} = 0.4$. At least one of these jets is required to have originated from a b quark by using an algorithm that identifies a long-lived B hadron through the presence of displaced vertex (b tag) [63].

Backgrounds to the $t\bar{t}$ signal arise from multi-jet QCD production (non-W), W production in association with jets (W + jets), and electroweak backgrounds (EWK) composed of diboson (WW, WZ, ZZ) and single top production. W + jets background events include jets with real b flavor as well as light flavor jets incorrectly identified as b jets. To remove the non-W backgrounds, where $\not{E}_T$

Table 4. **Event selection criteria [64]**

Lepton	$E_T > 20$ GeV (electron, muon), $|\eta| < 1$
Jets	Exactly 4 with $E_T > 15$ GeV, $|\eta| < 2.0$
$\not{E}_T$	> 20 GeV, calculated over $|\eta| < 3.6$
b-tag jets	$\geqslant 1$ from a secondary vertex, $|\eta| < 1.5$
Non-W veto	$0.5 \leqslant \Delta\varphi \leqslant 2.5$ when $\not{E}_T < 30$ GeV$/c^2$

Table 5. **Background composition and expected number of $t\bar{t}$ candidates. All uncertainties are statistical only**

Source	Expected number of events
$W+$jets	14.5 ± 5.1
Non-W	5.2 ± 2.6
EWK	2.2 ± 0.5
Total	22.0 ± 8.2
$t\bar{t}$ ($\sigma = 8.0$ pb, $m_t = 170$ GeV$/c^2$)	145.1 ± 16.5
Data	167

is due to mismeasured jet energies, it was required $\not{E}_T$ not to be aligned with the highest energy jet by a suitable requirement on $\Delta\varphi$ between this jet and $\not{E}_T$. Table 4 summarizes the selection criteria used in this analysis, and a more detailed description can be found in [64]. There were selected 167 events of which one expected about 85% to be $t\bar{t}$ events. Table 5 shows the expected sample composition from a previous $t\bar{t}$ production analysis with 318 pb^{-1} [41,65], scaled to 955 pb^{-1} and assuming a $t\bar{t}$ cross section of 8.0 pb.

The method applied for analyses of the data is almost identical to that used in preceding section. Authors analyze the selected events using the likelihood technique that relies on calculations of probability densities based on matrix elements for the signal $t\bar{t}$ and dominant background ($W+$jets) processes [41,65]. The backgrounds other than $W+$jets are found to be adequately described by the $W+$jets probability density. Given a set of observed variables, x, and underlying partonic quantities, y, the signal and background probability densities are constructed by integrating over the appropriate parton level differential cross section, $d\sigma(y)/dy$ convolved with parton distribution functions (PDF) and detector resolution effects:

$$P(x) = \sum_{\text{jet perm}} \int \frac{d\sigma(y)}{dy} f(q_1) f(q_2) \, dq_1 \, dq_2 W(x,y) dy. \qquad (4)$$

The PDFs ($f(q_1)$ and $f(q_2)$) take into account the flavors of colliding quark and antiquark and are given by CTEQ5L [52]. The detector resolution effects are described by a transfer function $W(x, y)$ relating x to y. The momenta of the leptons and the angles of jets and leptons are taken to be exactly measured, and therefore $W(x, y)$ for these quantities is given by the product of Dirac delta functions. The nontrivial part of $W(x, y)$ maps parton energies to measured jet energies after correction for instrumental detector effects [56]. This mapping is obtained by parameterizing the jet response in fully simulated $t\bar{t}$ events created by the Monte Carlo (MC) generator PYTHIA [73], and including the effects of radiation, hadronization, measurement resolution, and energy omitted from the jet cone by the reconstruction algorithm. The $t\bar{t}$ and $W+$jets probability densities, $P_{t\bar{t}}$ and $P_{W+\text{jets}}$, include all possible permutations of matching jets with partons as well as all possible longitudinal momenta for the neutrino in the W decay. The permutations are reduced to six or two by exploiting b-tagging information (single-tag or double-tag, respectively). Different transfer functions were used for light quark jets and b jets, depending on the flavor of the parton assigned to the jet. In calculating $d\sigma(y)/dy$, $P_{t\bar{t}}$ uses the leading order matrix element of the $q\bar{q} \to t\bar{t}$ process [74], and $P_{W+\text{jets}}$ uses the sum of matrix elements of the $W + 4$ jets subroutines encoded in the VECBOS Monte Carlo generator [66].

The final state described by $d\sigma(y)/dy$ contains 6 particles, which introduces 20 integration variables in Eq. (4), including the longitudinal momenta of the incoming quarks. By imposing energy-momentum conservation, in conjunction with the Dirac delta functions in $W(x, y)$, the dimensionality of the remaining integration is reduced to five. The integration in $P_{W+\text{jets}}$ is performed over the energies of the outgoing partons and the invariant mass of the leptonically decaying W using a Monte Carlo technique. In order to reduce the calculation time for $P_{t\bar{t}}$, authors integrate over the following variables: the invariant masses of $t, \bar{t}, W^+$, and W^-, and the energy of one of the quarks from the hadronic W decay. The method includes two additional integrations over the transverse momentum components of the $t\bar{t}$ system. The integration in $P_{t\bar{t}}$ uses the numerical integration code VEGAS [67].

The largest potential systematic uncertainty in this measurement arises from the energy scale of jets. To decrease this uncertainty, authors exploit the fact that the hadronically decaying W provides an *in situ* constraint of the jet energy scale, as the two jets should form an invariant mass consistent with the precisely known mass of the W boson. The jet energy scale and the mass of the top quark are simultaneously determined from a two-dimensional likelihood that includes their correlation. A salient feature of this method is that the uncertainty due to the jet energy scale will be reduced with increasing statistics. Thus, P is evaluated as a function of m_t and an assumed jet energy scale factor $f_{\text{JES}} = E_{\text{jet}}^{\text{obs}}/E_{\text{jet}}$, where $E_{\text{jet}}^{\text{obs}}$ is the observed jet energy and E_{jet} is the true jet energy.

To extract m_t and f_{JES} from the data, it is necessary to build a likelihood function for N selected events by adding $P_{t\bar{t}}$ and $P_{W+\mathrm{jets}}$ for each event. The combined likelihood is minimized with respect to three variables: m_t, f_{JES}, and C_s, the fraction of events consistent with the $t\bar{t}$ signal hypothesis. The likelihood for N events is given by

$$\mathcal{L}(x_1, x_2, \ldots, x_N; m_t, f_{\mathrm{JES}}, C_s) =$$
$$= \exp\left[-N(C_s\langle A_{t\bar{t}}(m_t, f_{\mathrm{JES}})\rangle) + (1 - C_s)\langle A_{W+\mathrm{jets}}(f_{\mathrm{JES}})\rangle\right] \times$$
$$\times \prod_{i=1}^{N}[C_s P_{t\bar{t}}(x; m_t, f_{\mathrm{JES}}) + (1 - C_s)P_{W+\mathrm{jets}}(x; f_{\mathrm{JES}})], \quad (5)$$

where the first factor arises from the Poisson extension of the likelihood and normalizes the combined event probability density, and $\langle A \rangle$ refers to the mean acceptance for $t\bar{t}$ or $W+$jets events. Authors use fully simulated MC $t\bar{t}$ and $W+$jets events to determine the functional form of $\langle A \rangle$. $P_{W+\mathrm{jets}}$ is evaluated at the central jet energy scale factor $f_{\mathrm{JES}} = 1$. The f_{JES} dependence of $P_{W+\mathrm{jets}}$ is determined by varying the input f_{JES} in MC event samples ($f_{\mathrm{JES}}^{\mathrm{MC}}$) and by parameterizing the average likelihood response as a function of f_{JES}. The m_t dependence of the theoretical leading order $t\bar{t}$ cross section was used to normalize $P_{t\bar{t}}$. Because of using a leading order matrix element to calculate $P_{t\bar{t}}$, it was found that $t\bar{t}$ events, where at least one of the four reconstructed jets cannot be matched to a parton from the $t\bar{t}$ decay within $\Delta R < 0.4$, behave like background events. As a consequence, a pure sample of $t\bar{t}$ events yields C_s of 0.8. The quoted C_s values are corrected for this effect. For each event $P_{t\bar{t}}$ is evaluated in increments of 2 GeV/c^2 in m_t and 0.02 in f_{JES}. At each point of this grid the entire sample of N events was fitted according to Eq. (4), and the most likely value of C_s is determined using MINUIT [68]. The optimal parameters m_t and f_{JES} are obtained by fitting the likelihood using a two-dimensional Gaussian. The statistical uncertainty on m_t includes the uncertainty on f_{JES}.

The performance of the analysis is tested by extracting m_t from MC pseudo-experiments containing $t\bar{t}$ signal samples with various input top-quark masses (m_t^{MC}) and background samples described in Table 5. The signal and electroweak background samples are generated using HERWIG [73]. The $W+$jets background is generated using ALPGEN [73] with hadronization and fragmentation done by HERWIG. The non-W background is extracted from an independent data sample. The CDF detector simulation processes all of the MC samples. Authors of [61] constructed pseudo-experiments of signal and background events by fluctuating the number of events around the values shown in Table 5. Figure 9, a shows that the fitted Gaussian mean m_t extracted from 200 pseudo-experiments per point is unbiased with respect to m_t^{MC} up to the statistical uncertainty 0.21, which is taken as a systematic uncertainty. Similar tests are performed for the
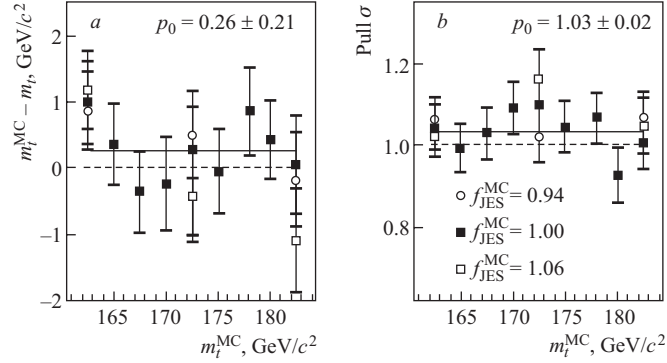
Fig. 9. Results of MC tests. *a*) Difference between the measured m_t and the input top-quark mass in the MC event sample (m_t^{MC}), as a function of m_t^{MC}. *b*) Gaussian σ of pull distributions (see text), as a function of m_t^{MC}. The plots include results using MC event samples with different values of f_{JES} ($f_{\mathrm{JES}}^{\mathrm{MC}}$). The weighted average p_0 is indicated by the solid horizontal line. The dashed line indicates an example of an unbiased result
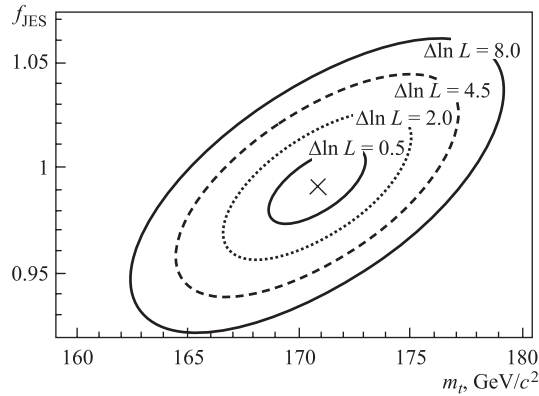

Fig. 10. Contours of likelihood evaluated over the 955 pb^{-1} event sample. The measurement is indicated by X

output of f_{JES}. In this case, there was found that a bias of $+4\%$ in f_{JES} is present, independent of m_t. This bias was corrected to properly interpret the output of f_{JES}. Figure 9, *b* shows the top-mass pull width, defined as the Gaussian σ of the top-mass residual ($m_t - m_t^{\mathrm{MC}}$) divided by the uncertainty in each pseudo-experiment σm_t, as a function of m_t^{MC}. The pull width is $(3 \pm 2)\%$ larger than one on average, and thus, the statistical uncertainty is scaled up by 3%.

Applying this method to data, the top-quark mass was measured to be $m_t = 170.8 \pm 2.2(\mathrm{stat.})$, and the f_{JES} scale to be $f_{\mathrm{JES}} = 0.99 \pm 0.02(\mathrm{stat.})$ in good agreement with the reference scale from the default CDF calibration [56]. Figure 10 shows the fitted two-dimensional likelihood with $\Delta \ln L$ contours.
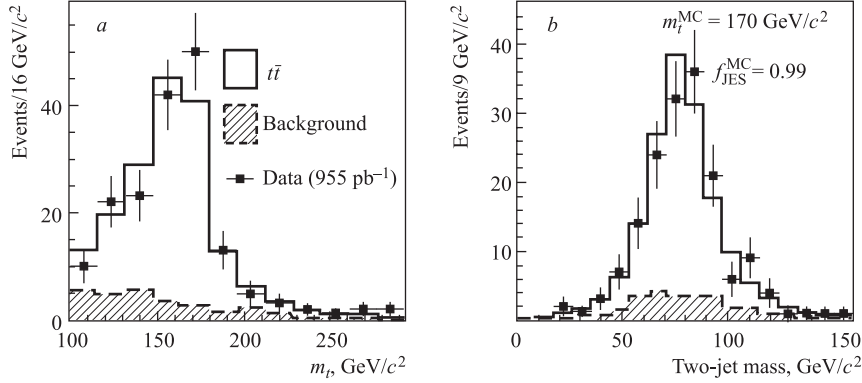
Fig. 11. Comparison of two kinematic variables for data and MC using $m_t^{\mathrm{MC}} = 0.99$ and $m_t^{\mathrm{MC}} = 170$ GeV/c^2. *a*) Most probable value of m_t for each event extracted from evaluating $P_{t\bar{t}}$ at $f_{\mathrm{JES}} = 1$. *b*) Invariant mass of the pair of jets assigned as W-decay products calculated using the most probable permutation at the most probable value of m_t and f_{JES} in each event evaluated from $P_{t\bar{t}}$. The backgrounds contain all contributions shown in Table 5

The statistical uncertainty is taken from the maximum and minimum m_t values on the $\Delta \ln L = 0.5$ contour. A correlation coefficient of 0.32 was found between m_t and f_{JES}. The fit yields a signal fraction $C_s = 0.84 \pm 0.10(\mathrm{stat.})$, which corresponds to (140 ± 17) $t\bar{t}$ events and is consistent with the expectation shown in Table 5. Monte Carlo tests have shown that the resulting m_t is stable over a wide range of sample purities. Figure 11 shows comparisons of two representative kinematic quantities between data and simulation using $f_{\mathrm{JES}}^{\mathrm{MC}} = 0.99$ and $m_t^{\mathrm{MC}} = 170$ GeV/c^2; the agreement is good.

The sources of systematic uncertainty are listed in Table 6. To first order, f_{JES} is already included in the statistical uncertainty, but there was also considered a dependence of f_{JES} on p_T and η of the jets (residual jet energy scale) using the dependence found in other studies [56]. Another uncertainty is calculated from possible differences in f_{JES} between b jets and light quark jets. The generator uncertainty takes into account differences in parton showering and jet fragmentation between two different MC programs used to generate $t\bar{t}$ events, PYTHIA and HERWIG. Variations in initial- and final-state radiation (ISR, FSR), constrained by studies using Drell–Yan data, are also considered [62]. PDF uncertainties are evaluated using MC samples generated with MRST [69] and the full set of eigenvectors from CTEQ6M [52].

Systematic effects on the modeling of the background samples include fluctuations in the total background contribution, relative contributions from individual background processes, and variations due to the Q^2 scale used in W+ jets sim-

Table 6. **Summary of systematic uncertainties**

Source	Uncertainty, GeV/c^2
Residual jet energy scale	0.4
b-jet energy scale	0.6
Generator	0.2
ISR/FSR	1.1
PDFs	0.1
Background composition	0.2
Lepton p_T	0.2
b tag p_T dependence	0.3
Monte Carlo statistics	0.2
Multiple interactions	0.1
Total	1.4

ulation. There were also included effects from the uncertainties in the simulated lepton p_T, the dependence of b tagging with jet p_T, and the effect of the limited MC event samples used in the analysis. Finally, a possible mismodeling of multiple interactions in the simulation at high luminosity was included. The sum in quadrature of all systematic uncertainties is 1.4 GeV/c^2.

In summary, authors [61] presented a measurement of the top-quark mass in the lepton + jets channel using 955 pb^{-1} of data collected by the CDF experiment. A matrix element analysis was used with an *in situ* measurement of the jet energy scale. The main result is

$$m_t = (170.8 \pm 2.2(\text{stat.}) \pm 1.4(\text{syst.})) \text{ GeV}/c^2,$$

where the statistical uncertainty includes the uncertainty of 1.5 GeV/c^2 due to the jet energy scale. With a total uncertainty of 1.5%, this result is the most precise measurement of the top-quark mass to date and is a 35% improvement over the previous best measurement [8, 10, 43, 62].

We have considered method based on matrix elements for the signal ($t\bar{t}$) and dominate background processes for two decay topologies: lepton plus jets and dilepton configurations. At integrated luminosity 1 fb^{-1} as well as for other luminosities, the first topology of the top-quark decay results in more precise data. This is well seen in Table 7, where are shown results of mass measurement considered in this review and rather precise, in our opinion, data that were obtained using other analysis methods. It is clear that it is necessary to probe different channels of investigation because of different backgrounds in the data. For instance, dilepton decay mode contains less admixture of background processes than other modes, though has significantly less statistics as compared with $l+$jets and all-hadronic modes.

Table 7. **The summary of top-quark mass measurements (published in summer 2008)**

Channel	Description	Top-quark mass measurement, GeV/c^2	Lumin. integr.	Reference
Lepton + jets	Dynamical likelihood method + b-tag	$173.2^{+2.6}_{-2.4}$ (stat.) ± 3.2(syst.)	318 pb^{-1}	Phys. Rev. D. 2006. V. 73. P. 092002
Lepton + jets	Template technique	$173.5^{+3.7}_{-3.6}$(stat.) ± 1.3(syst.)	318 pb^{-1}	Phys. Rev. D. 2005. V. 72. P. 032003
Lepton + jets	Matrix element with in situ $W \to 2$ jets JES calibration	170.9 ± 2.2(stat.) ± 1.4(syst.)	1 fb^{-1}	Phys. Rev. Lett. 2007. V. 99. P. 182002
Dilepton	Matrix element	164.5 ± 3.9(stat.) ± 3.9(syst.)	1 fb^{-1}	Phys. Rev. D. 2007. V. 75. P. 031105
Dilepton	$M_{\rm rec}$ template + $t\bar{t}P_z$ with cross section constraint	$169.7^{+5.2}_{-4.9}$ (stat.) ± 3.1(syst.)	1.2 fb^{-1}	Phys. Rev. Lett. 2008. V. 100. P. 062005
All-hadronic	Template technique	174.0 ± 2.2 (stat.) ± 4.8(syst.)	1 fb^{-1}	Phys. Rev. D. 2007. V. 76. P. 072009
Tevatron combined	CDF & D∅	172.4 ± 0.7 (stat.) ± 1.0(syst.)	2.8 fb^{-1}	hep-ex/0808.1089

3. NEW PHENOMENA OBSERVED AT CDF EXPERIMENT

3.1. Discovery of $B_S^0 - \bar{B}_S^0$ Oscillations. Like B_d^0 mesons, B_S mesons oscillate from particle to antiparticle due to flavor changing weak interactions with a frequency proportional to the mass difference Δm_s between the two mass eigenstates, B_S^H and B_S^L (if $h = c = 1$ is set, $\Delta m_s = m_s^H - m_s^L$ is in inverse picoseconds). The probability density for a $\bar{B}_S^0$ meson produced at time $t = 0$ to decay at proper time t in the same state, or to be mixed to the $\bar{B}_S^0$ state is given by

$$P_{\rm nomix}(t) = \frac{\Gamma_s}{2} e^{-\Gamma_s t} [1 + \cos(\Delta m_s t)],$$

$$P_{\rm mix}(t) = \frac{\Gamma_s}{2} e^{-\Gamma_s t} [1 - \cos(\Delta m_s t)],$$

where Γ_s is the decay width assumed to be equal for the two mass eigenstates, and effects from CP violation are neglected.

The mass differences $\Delta m_d = m_d^H - m_d^L$ and Δm_s can be used to determine the fundamental parameters $|V_{td}|$ and $|V_{ts}|$ of the Cabibbo–Kobayashi–Maskawa (CKM) matrix, which relates the quark mass eigenstates to the flavor eigenstates. Although, in principle, only Δm_d is necessary to extract the CKM matrix element $|V_{td}|$, this determination, however, has large theoretical uncertainties. A measurement of Δm_s combined with $\Delta m_d = (0.505 \pm 0.05)$ ps^{-1}, obtained at B factories [79], would determine the ratio $|V_{td}/V_{ts}|$ with a significantly smaller theoretical uncertainty, contributing to a stringent test the unitarity of the CKM matrix. Therefore, the measurement of Δm_s was one of major objectives of particle physics since the first observations of $B^0 - \bar{B}^0$ transformation in 1987 by UA1 and ARGUS collaborations [70]. Those consisted of a time-integrated analysis based on the measurement of the ratio of like sign muon pairs to unlike sign muon pairs. Time-integrated methods have two drawbacks: 1) at $p\bar{p}$ collider or at the Z^0 resonance both B_d^0 and B_S^0 mesons are produced and they are not known very precisely; 2) the time-integrated mixing probability is not very sensitive to $\Delta m_s/\Gamma_s$, if $\Delta m_s/\Gamma_s$ is larger than about 3.

Better sensitivity is obtained with the time-dependent analysis aiming at the direct measurement of the oscillation frequency Δm_s from the proper time distributions of B_S^0 candidates identified through their decay in flavor-specific modes and suitably tagged as mixed or unmixed. This requires, however, a well-functioning high resolution vertex detector.

Earlier time-dependent measurements of Δm_s performed at LEP and SLD operating at the Z pole, and at CDF in Run I have yielded a lower limit $\Delta m_s > 14.5$ ps^{-1} at the 95% CL [71]. First two-sided limits, $17 < \Delta m_s < 21$ ps^{-1}, were reported in 2006 by D∅ [72] with significance of 2.5σ (90% CL). In the same year, CDF published the first direct measurements of Δm_s and $|V_{td}/V_{ts}|$, using about 1 fb^{-1} of integral luminosity [73]:

$$\Delta m_s = (17.31^{+0.33}_{-0.18}(\text{stat.}) \pm 0.07(\text{syst.})) \text{ ps}^{-1},$$
$$|V_{td}/V_{ts}| = 0.208^{+0.001}_{-0.002}(\text{exp.})^{+0.008}_{-0.006}(\text{theor.}).$$

The sample contained 3600 fully reconstructed hadronic B_S decays and 37 000 partially reconstructed semileptonic decays*.

Before long in 2006 CDF printed the second paper with more precise result [74]. Using the same data sample of 1 fb^{-1}, authors have found signals of 5600 fully reconstructed and 3100 partially reconstructed hadronic B_S decays, and 61 500 partially reconstructed semileptonic B_S decays.

---

*The symbol B_S refers to the combination of B_S^0 and $\bar{B}_S^0$ decays. References to a particular process imply that the charge conjugate process is included as well.

The result is

$$\Delta m_s = (17.77 \pm 0.10(\text{stat.}) \pm 0.07(\text{syst.})) \text{ ps}^{-1},$$
$$|V_{td}/V_{ts}| = 0.2060 \pm 0.0007(\text{exp.})^{+0.0081}_{-0.0060}(\text{theor.}).$$

They measured the probability that B_S decays with the same, or opposite flavor to the flavor at production point as a function of proper decay time and have found a significant signal of $B_S^0 - \bar{B}_S^0$ oscillations. The probability that random fluctuations would produce a comparable signal is $8 \cdot 10^{-8}$, which exceeds 5σ signal significance. This is the first definitive observation of time-dependent $B_S^0 - \bar{B}_S^0$ oscillations. The measured value of Δm_s allows one to determine $|V_{td}/V_{ts}|$ with unprecedented precision.

The key components of the CDF II detector for this measurement are as follows. Precision determination of the decay point is provided by a seven-layer double-sided silicon-strip detector and a single-sided layer of silicon mounted directly on the beam pipe at an average radius of 1.5 cm. A 96-layer drift chamber, (COT), is used for both precision tracking and dE/dx particle identification. Time-of-flight (TOF) counters surrounding the drift chamber are used to identify low-momentum charged kaons. A three-level trigger system selects, in real time, $p\bar{p}$ collisions containing charm and bottom hadrons by exploiting the kinematics of production and decay, and the long lifetimes of D and B mesons. A crucial component of the trigger system for this measurement is the Silicon Vertex Trigger [25–32], which makes it possible to collect large sample of B_S mesons in the fully or partially reconstructed hadronic decay modes, giving CDF unique sensitivity to B_S oscillations.

To identify the flavor of B_S at production, authors use characteristics of b-quark production and fragmentation in $p\bar{p}$ collisions. In a simple model of fragmentation, a b quark becomes a $\bar{B}_S^0$ meson when some of the energy of the b quark is used to produce a $s\bar{s}$-quark pair. The b and the $\bar{s}$ bind to form a $\bar{B}_S^0$. The remaining s quark may form a K^-. Similarly, a $\bar{b}$ that becomes a B_S^0 is accompanied by a K^+. One of the two techniques used to identify the production flavor of B_S is based on the charge of these kaons (same-side tag). The second technique uses the charge of the lepton from semileptonic decays or a momentum-weighted charge of the decay products of the second b hadron produced in the collision (opposite-side tag).

The analysis was upgraded as compared with [73] by increasing the B_S signal yield and improving the performance of the methods used to identify the flavor (b or $\bar{b}$) of B_S at production. The previous analysis used B_S decays in hadronic ($\bar{B}_S^0 \to D_S^+ \pi^-, D_S^+ \pi^- \pi^+ \pi^-$) and semileptonic ($\bar{B}_S^0 \to D_S^{+(*)} \ell^- \bar{\nu}_\ell, \ell = e, \mu$) decay modes; authors [74] also used hadronic decays $D_S^+ \to \varphi \pi^+, \bar{K}^*(892)^0 K^+$, and $\pi^+ \pi^- \pi^+$ with $\varphi \to K^+ K^-$ and $\bar{K}^{*0} \to K^- \pi^+$. Several improvements lead to increased signal yields. Particle identification techniques were used to

find kaons from D_S-meson decays, allowing one to relax kinematic selection requirements on the D_S-decay products. This results in increased efficiency for D_S reconstructing while maintaining excellent signal-to-background ratio. In the hadronic channels, authors employ an artificial neural network (ANN) to improve candidate selection resulting in larger signal yields at similar or smaller background levels. The ANN selection makes it possible to use the additional decay sequence $\bar{B}_S^0 \to D_S^+ \pi^- \pi^+ \pi^-$ with $D_S^+ \to \pi^+ \pi^- \pi^+$ as well. They add significant statistics using partially reconstructed hadronic decays in which a photon or π^0 is missing: $\bar{B}_S^0 \to D_S^{*+} \pi^-$, $\breve{D}_S^{*+} \to D_S^+ \gamma/\pi^0$ and $\bar{B}_S^0 \to D_S^+ \rho^-$, $\rho^- \to \pi^- \pi^0$, with $D_S^+ \to \varphi \pi^+$. Finally, ANN is used to enhance the performance of the methods used to identify the flavor of B_S at production. With all these improvements, the effective statistical size of the data sample is increased by a factor of 2.5.

To reconstruct $\bar{B}_S^0$ candidates, first there were selected D_S^+ candidates. These D_S^+ candidates are combined with one or three additional charged particles to form $D_S^+ \ell^-$, $D_S^+ \pi^-$ or $D_S^+ \pi^- \pi^+ \pi^-$ candidates. In the previous analysis [73], authors reduced combinatorial backgrounds by applying requirements on selection quantities such as the minimum p_T of $\bar{B}_S^0$ and its decay products, and the quality of the reconstructed B^0 and D_S^+ decay points and their displacement from the $p\bar{p}$-collision position. In this analysis, authors of [74] add kaon identification likelihood formed from TOF and dE/dx information. For decay modes with kaons in the final state, there was used this likelihood to reduce combinatorial background from random pions or physics backgrounds such as $D^+ \to K^- \pi^+ \pi^+$. In [73], D_S^+ candidates consistent with the D^+-mass hypothesis were vetoed, which resulted in a substantial loss of signal efficiency. Kaon identification makes it possible to relax kinematic requirements (charged particle p_T and the D^+ veto) leading to a substantial increase in signal efficiency. In the semileptonic channel, the main gain is in the $D_S^+ \ell^-$, $D_S^+ \to \bar{K}^*(892)^0 K^+$ sequence, where the signal is increased by a factor of 2.2. An additional gain in signal by a factor of 1.3 with respect to previous analysis comes from adding data selected with different trigger requirements. In total, the signal of 37 000 semileptonic B_S decays in [73] is increased to 61 500, and the signal to background improves by a factor of two in the sequences with kaons in the final state. The distributions of the invariant masses of the $D_S^+(\varphi \pi^+) \ell^-$ pairs $m_{D_S \ell}$ and the $D_S^+(\varphi \pi^+)$ candidates are shown in Fig. 12, a; $m_{D_S \ell}$ was used to help distinguish signal, which occurs at higher $m_{D_S \ell}$ from combinatorial and physics (e.g., double-charm decays of B mesons) backgrounds.

In the hadronic decay modes, an ANN was used to enhance the signal selection of the previous analysis. The ANN uses quantities such as the selection criteria listed above as well as the kaon identification likelihood. The network is trained using simulated signals generated with Monte Carlo method.
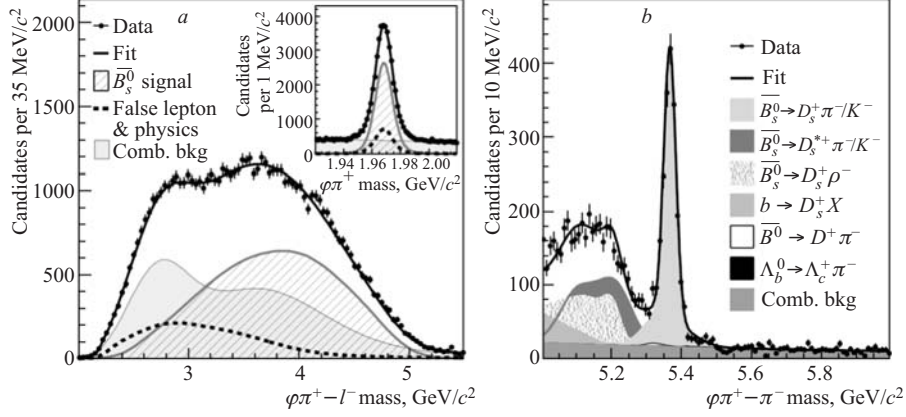
Fig. 12. *a*) The invariant mass distributions for the D_S^+ ($\varphi\pi^+$) candidates (inset) and the $\ell^- D_S^+$ ($\varphi\pi^+$) pairs. The contribution labeled «false lepton & physics» refers to backgrounds from hadrons mimicking the lepton signature combined with real D_S mesons and physics backgrounds such as $B^0 \to D_S^+ D^-$, $D_S^+ \to \varphi\pi^+$, $D^- \to \ell^- X$. *b*) The invariant mass distribution for $\bar{B}_S^0 \to D_S^+ (\varphi\pi^+)\pi^-$ decays including the contributions from $B_S^0 \to D_S^{*+}\pi^-$ and $\bar{B}_S^0 \to D_S^+\rho^-$. In this panel, signal contributions are drawn added on top of the combinatorial background

For combinatorial background were used sideband regions in the mass distribution of the B_S candidates from data. In this analysis [74], authors add the partially reconstructed signal between 5.0 and 5.3 GeV/c^2 from $\bar{B}_S^0 \to D_S^{*+}\pi^-$, $D_S^{*+} \to D_S^+\gamma/\pi^0$ in which a photon or π^0 from D_S^{*+} is missing and $\bar{B}_S^0 \to D_S^+\rho^-$, $\rho^- \to \pi^-\pi^0$ in which a π^0 is missing. The mass distributions for $\bar{B}_S^0 \to D_S^+\pi^-$, $D_S^+ \to \varphi\pi^+$ and the partially reconstructed signals are shown in Fig. 12, *b*. The mass distributions for the other five hadronic decay sequences are shown in Fig. 13. In these modes, the masses of the candidates were required to be greater than 5.3 GeV/c^2. Candidates with masses greater than 5.5 GeV/c^2 are used to construct probability density functions (PDFs) for combinatorial background. Table 8 summarizes the signal yields.

The reconstructed decay time in the B_S rest frame is $t = m_{B_S} L_T / p_T^{\mathrm{recon}}$, where L_T is the displacement of the B_S-decay point with respect to the primary vertex projected onto the B_S transverse momentum vector, and p_T^{recon} is the transverse momentum of the reconstructed decay products. In the semileptonic and partially reconstructed hadronic decays, t was corrected by a factor $k = p_T^{\mathrm{recon}}/p_T(B_S)$ determined with Monte Carlo simulation (Fig. 13).

The distribution of resolution σ_t for fully reconstructed decays has an average value of 87 fs, which corresponds to one fourth of an oscillation period at $\Delta m_s = 17.8$ ps^{-1}. The distribution is nearly Gaussian with an rms width of 31 fs. For
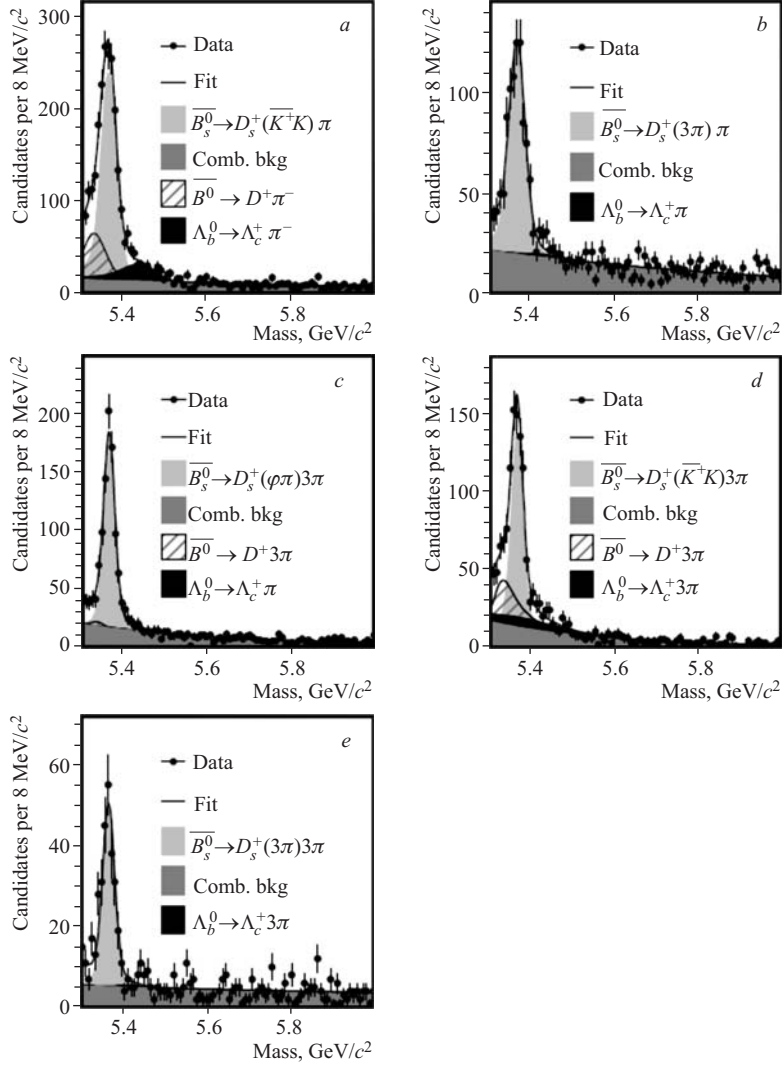
Fig. 13. The invariant mass distributions for $\bar{B}_S^0 \rightarrow D_S^+ \pi^-$ $(D_S^{*+} \rightarrow D_S^+ \gamma/\pi^0)$ (a, b) and $D_S^+ \pi^- \pi^+ \pi^-$ (c, d, e). Signal contributions are added on top of the combinatorial background. Contributions from partially reconstructed B_S decays are taken into account in the fit and are not shown

the partially reconstructed hadronic decays, the average σ_t is 97 fs, and the addition to σ_t due to the missing photon or π^0 is very small (Fig. 13). For semileptonic decays, σ_t is worse due to decay topology and the much larger

Table 8. **Signal yields (S) and signal-to-background ratio (S/B) in the various hadronic decay sequences. The gain refers to the percentage increase in $S/\sqrt{S+B}$ relative to [73]**

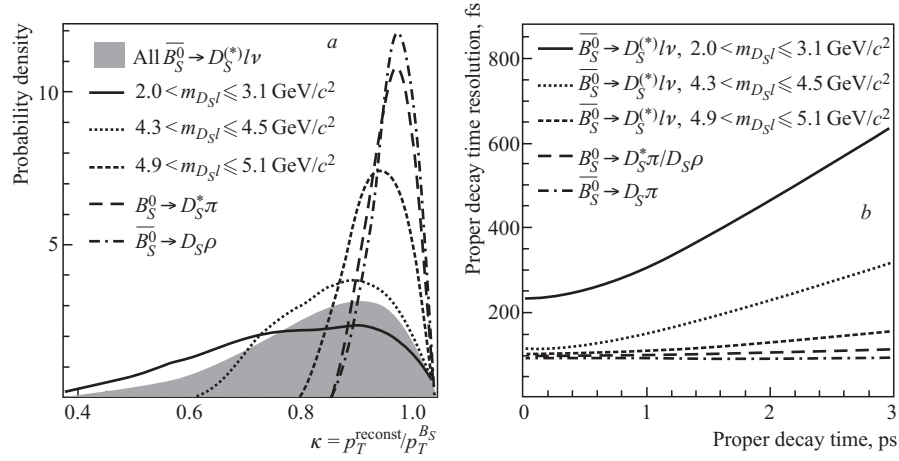| Decay sequence	Signal	S/B	Gain,% [73]
$\bar{B}_S^0 \to D_S^+(\varphi\pi^+)\pi^-$	2000	11.3	13
Partially reconstructed	3100	3.4	N.a.
$\bar{B}_S^0 \to D_S^+(\bar{K}^*(892)^0 K^+)\pi^-$	1400	2.0	35
$\bar{B}_S^0 \to D_S^+(\pi^+\pi^-\pi^+)\pi^-$	700	2.1	22
$\bar{B}_S^0 \to D_S^+(\varphi\pi^+)\pi^-\pi^+\pi^-$	700	2.7	92
$\bar{B}_S^0 \to D_S^+(K^*(892)^0 K^+)\pi^-\pi^+\pi^-$	600	1.1	110
$\bar{B}_S^0 \to D_S^+(\pi^+\pi^-\pi^+)\pi^-\pi^+\pi^-$	200	2.6	N.a.

Fig. 14. *a*) The distribution of the correction factor κ in semileptonic and partially reconstructed hadronic decays from Monte Carlo simulation. *b*) The average proper decay time resolution for B_S decays as a function of proper decay time

missing momentum of decay products that were not reconstructed. The increase of σ_t with t is illustrated in Fig. 14 for different ranges of $m_{D_S\ell}$.

The flavor of B_S at production is determined using both opposite-side and same-side flavor tagging techniques. The effectiveness $Q \equiv \varepsilon D^2$ of these techniques is quantified with efficiency ε, the fraction of signal candidates with a flavor tag, and a dilution $D \equiv 1 - 2\omega$, where ω is the probability that the tag is incorrect.

In the previous analysis, were used lepton (e and μ) charge and jet charge as tags, and if both types of tag were present, the lepton tag was used. In this improved analysis, authors add an opposite-side flavor tag based on the charge

of identified kaons, and combine the information from the kaon, lepton, and jet charge tags using an ANN. The dilution is measured in data [75] using large samples of B^-, which do not change flavor, and $\bar{B}^0$, which can be used after accounting for their well-known oscillation frequency. The combined opposite-side tag effectiveness improves by 20% to $Q = (1.8 \pm 0.1)\%$. Most of the improvements is for candidates with both a lepton and a jet-charge tag.

As we have mentioned above, same-side flavor tags are based on the charges of associated particles produced in the fragmentation of the b quark that produces the reconstructed B_S. In the previous analysis, a same-side tag based on kaon particle-identification likelihood was used; here authors use an ANN to combine kaon particle-identification likelihood with kinematics quantities of the kaon candidate into a single tagging variable T. Tracks close in phase space to the B_S candidate are considered as same-side kaon tag candidates, and the track with the largest value of T is selected as the tagging track. The dilution of the same-side tag was predicted using simulated data samples generated with the PYTHIA Monte Carlo [55] program. The predicted fractional gain in Q from using the ANN is 10%. Control samples of B^- and $\bar{B}^0$ are used to validate the predictions of the simulation. The effectiveness of this flavor tag increases with p_T of $\bar{B}^0_S$; there was found $Q = 3.7\%$ (4.8%) in the hadronic (semileptonic) decay sample. The fractional uncertainty on Q is approximately 25% [73]. If both a same-side tag and an opposite-side tag are present, then the combined information from both tags is used assuming they are independent.

The signal PDF has the general form:

$$S_{\pm}(t_i, \sigma_{t_i}, D_i) = \varepsilon(t_i) \int \frac{\Gamma_s}{2} e^{-\Gamma_s t'} [1 + AD_i \cos(\Delta m_s t')] \, G(t_i - t', \sigma_{t_i}) \, dt',$$

where D_i is the ith candidate dilution; t_i is a reconstructed decay time; σt_i — width of a Gaussian distribution $G(x - \mu, \sigma)$ with mean μ; $\varepsilon(t)$ is decay time efficiency function which describes trigger and selection biases and is determined from Monte Carlo simulation. Following the method described in [77], fit for the oscillation amplitude was used while fixing Δm_s to a probe value. The oscillation amplitude is expected to be consistent with $A = 1$ when the probe value is the true oscillation frequency, and consistent with $A = 0$ when the probe value is far from the true oscillation frequency. An unbinned maximum likelihood fit was used to search for B_S oscillations. The likelihood combines mass, decay time, decay-time resolution, and flavor tagging information for each candidate, and includes terms for signal and each type of background. Details of the fit are described in [73, 76].

Figure 15 shows the fitted value of the amplitude as a function of the oscillation frequency for the semileptonic candidates alone, the hadronic candidates alone, and the combination. The sensitivity [73, 77] is 19.3 ps^{-1} for the semileptonic decays alone, 30.7 ps^{-1} for the hadronic decays alone, and
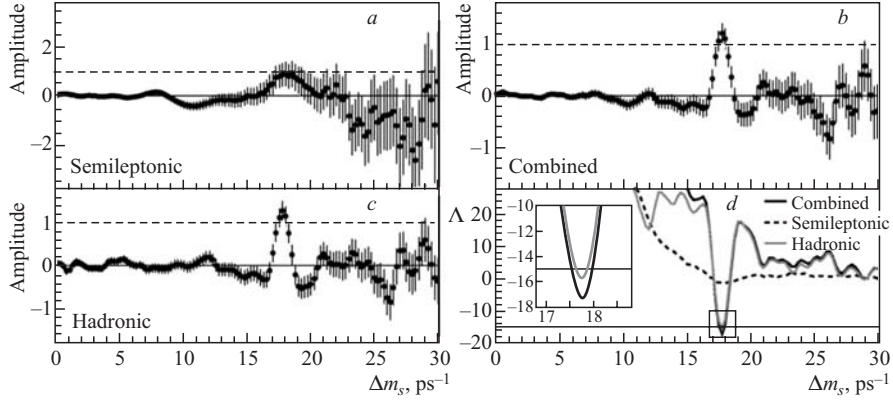
Fig. 15. The measured amplitude values and uncertainties versus the $B_S^0 - \bar{B}_S^0$ oscillation frequency Δm_s. *a*) Semileptonic decays only. *b*) All decay modes combined. *c*) Hadronic decays only. *d*) The logarithm of the ratio of likelihoods for amplitude equal to one and amplitude equal to zero, $\Lambda \equiv \log |L^{A=0}/L^{A=1}(\Delta m_s)|$, versus the oscillation frequency. The horizontal line indicates the value $\Lambda = -15$ that corresponds to a probability of $5.7 \cdot 10^{-7}$ (5σ) in the case of randomly tagged data

31.3 ps^{-1} for all decays combined. At $\Delta m_s = 17.75$ ps^{-1}, the observed amplitude $A = 1.21 \pm 0.20$(stat.) is consistent with unity, indicating that the data are compatible with $B_S^0 - \bar{B}_S^0$ oscillations with that frequency, while the amplitude is inconsistent with zero: $A/\sigma A = 6.05$, where σA is the statistical uncertainty on A (the ratio has negligible systematic uncertainties). The small uncertainty on A at $\Delta m_s = 17.75$ ps^{-1} is due to the superior decay-time resolution of the hadronic decay modes. The significance of the signal was evaluated using $\Lambda \equiv \log |L^{A=0}/L^{A=1}(\Delta m_s)|$, which is the logarithm of the ratio of likelihoods for the hypothesis of oscillations $A = 1$ at the probe value and the hypothesis that $A = 0$ which is equivalent to random production flavor tags. Figure 15 shows Λ as a function of Δm_s. Separate curves are shown for the semileptonic data alone (dashed), the hadronic data alone (light solid), and the combined data (dark solid). At the minimum $\Delta m_s = 17.75$ ps^{-1}, $\Lambda = -17.26$. The significance of the signal is the probability that randomly tagged data would produce a value of Λ lower than –17.26 at any value of Δm_s. Authors [73] repeat the likelihood scan 350 million times with random tagging decisions; 28 of these scans have $\Lambda < -17.26$ corresponding to a probability of $8 \cdot 10^{-8}$ (5.4_σ), well below $5.7 \cdot 10^{-7}$ (5_σ).

To measure Δm_s authors fix $A = 1$ and fit for the oscillation frequency. They find

$$\Delta m_s = (17.77 \pm 0.10(\text{stat.}) \pm 0.07(\text{syst.})) \text{ ps}^{-1}.$$

The only non-negligible systematic uncertainty on Δm_s is from the uncertainty on the absolute scale of the decay-time measurement. Contributions to this

uncertainty include biases in the primary vertex reconstruction due to the presence of the opposite-side b hadron, uncertainties in the silicon detector alignment, and biases in track fitting. The uncertainty on the correction κ for the hadronic candidates with a missing photon or π^0 is included and has a negligible effect.

The $B_S^0 - \bar{B}_S^0$ oscillations are depicted in Fig. 16. Candidates in the hadronic sample are collected in five bins of proper decay-time modulo of the measured oscillation period $2\pi/\Delta m_s$. In each bin, the fit for an amplitude was made (the points in Fig. 16) using the likelihood function [73], which takes into account the effects of background, flavor tag dilution and decay-time resolution for each candidate. The curve shown in Fig. 16 is a cosine with amplitude of 1.28, which is the observed value in the amplitude scan for the hadronic sample at $\Delta m_s = 17.77$ ps^{-1}. As expected, the data are well represented by the curve. The measured oscillation frequency is used to derive the ratio $|V_{td}/V_{ts}| = \xi\sqrt{\dfrac{\Delta m_d}{\Delta m_s}\dfrac{m_{B_S^0}}{m_{B^0}}}$ [79].

Fig. 16. The $B_S^0 - \bar{B}_S^0$ oscillation signal measured in five bins of proper decay-time modulo of the measured oscillation period $2\pi/\Delta m_s$. The figure is described in the text

As inputs $m_{B^0}/m_{B_S^0}$ [77] was used with negligible uncertainty $\Delta m_d = (0.507 \pm 0.005)$ ps^{-1} [79] and $\xi = 1.21_{-0.035}^{+0.047}$ [80]. Authors find $|V_{td}/V_{ts}| = 0.2060 \pm 0.0007(\text{exp.})_{-0.0060}^{+0.0081}(\text{theor.})$.

In conclusion, the first observation of oscillations $B_S^0 - \bar{B}_S^0$ from a decay-time dependent measurement of Δm_s was reported. The signal exceeds 5σ significance and yields a precise value of Δm_s which is consistent with Standard Model expectations.

3.2. Heavy Baryons. First search for baryon containing heavy b quark naturally was Λ_b^0. The Fermilab Tevatron has accumulated the world's largest sample of fully reconstructed Λ_b^0 baryons. It became possible due to the large b-production cross section in $p\bar{p}$ collisions at $\sqrt{s} = 1.96$ TeV and the ability of the CDF II experiment to select by SVT trigger fully hadronic decays of b hadrons. Recently (2006), CDF II [78] has brought the most precise measurement of the mass: $m(\Lambda_b^0) = (5619.7 \pm 1.2 \pm 1.2)$ MeV/c^2. (This value has the precision greater than PDG average 2008.) All this opens also a new possibility of investigation of other heavy baryons, which may consist of b and lighter quarks u, d, s, c, and some of these indeed were discovered. We consider below first observations of Σ_b and Ξ_b particles, which were observed recently with the help of the CDF II detector.
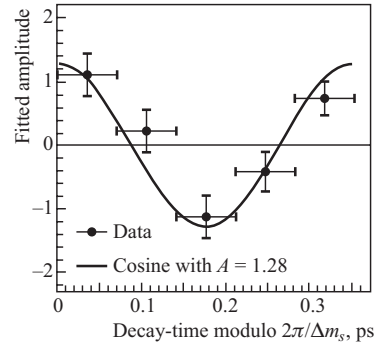
3.3. First Observation of Heavy Baryons Σ_b **and** Σ_b^***.** The world's largest sample of fully reconstructed Λ_b^0 baryons, accumulated with the CDF II detector, contains 3180 ± 60(stat.) $\Lambda_b^0 \to \Lambda_c^+ \pi^-$ candidates. Authors [81] presented an observation of four $\Lambda_b^0 \pi^\pm$ resonances, where $\Lambda_b^0 \to \Lambda_c^+ \pi^-$ and $\Lambda_c^+ \to pK^- \pi^+$, using 1.1 fb^{-1} of data. The $\Lambda_b^0 \pi$ states are interpreted as the lowest-lying charged Σ_b baryons and will be labeled $\Sigma_b^{(*)}$. The symbol Σ_b refers to $\Sigma_b^\pm$, while $\Sigma_b^{(*)}$ refers to $\Sigma_b^{*\pm}$. Any reference to a specific charge state implies the antiparticle state as well.

The Σ_b^{*+} baryons contain one b and two u quarks, while the Σ_b^{*-} baryons contain one b and two d quarks; these states are expected to exist but have not been observed. Baryons containing one bottom quark and two light quarks can be described by heavy-quark effective theory (HQET) [82]. In HQET a bottom baryon consists of a b quark acting as a static source of the color field surrounded by a diquark system comprised of the two light quarks. In the lowest-lying $\Sigma_b^{(*)}$ states, the diquark system has strong isospin $I = 1$ and $J^p = 1^+$, which couple to the heavy-quark spin and result in a doublet of baryons with $J^p = 1/2^+ (\Sigma_b)$ and $J^p = 3/2^+ (\Sigma_b^{(*)})$. This doublet is degenerate for infinite b-quark mass. As the b-quark mass is finite, there is a hyperfine mass splitting between the $3/2^+$ and $1/2^+$ states. There is also an isospin mass splitting between the $\Sigma_b^{(*)-}$ and $\Sigma_b^{(*)+}$ states.

Predictions for the $\Sigma_b^{(*)}$ masses come from nonrelativistic and relativistic potential quark models [83], $1/N_C$ expansion [84], quark models in the HQET approximation [85], sum rules [86], and lattice quantum chromodynamics calculations [87].

According to [83–87], one can expect $m(\Sigma_b) - m(\Lambda_b^0) \sim 180–210$ MeV/c^2, $m(\Sigma_b^*) - m(\Sigma_b) \approx 10–40$ MeV/c^2, and $m(\Sigma_b^{(*)-}) - m(\Sigma_b^{(*)+}) \sim 5–7$ MeV/c^2. The difference between the isospin mass splitting of the Σ_b^* and Σ_b multiplets is predicted to be $|m(\Sigma_b^{*+}) - m(\Sigma_b^{*-})| - |m(\Sigma_b^+) - m(\Sigma_b^-)| = (0.40 \pm 0.07)$ MeV/c^2 [88].

The natural width of Σ_b^* baryons is expected to be dominated by the P-wave one-pion transition $\Sigma_b^{(*)} - \Lambda_b^0 \pi$, whose partial width depends on the available phase space and the pion coupling to a constituent quark. Using an HQET prediction [89], the natural widths for the expected $\Sigma_b^{(*)}$ masses are $\tilde{A}(\Sigma_b^\pm) \approx 7$ MeV/c^2 and $\Gamma(\Sigma_b^{*\pm}) \approx 13$ MeV/c^2.

In reconstructing the decays $\Lambda_b^0 \to \Lambda_c^+ \pi^-$ and $\Lambda_c^+ \to pK^- \pi^+$, the proton from the Λ_c^+ decay and π^- from the Λ_b^0 decay both must have $p_T > 2$ GeV/c, while the K^- and π^+ candidates have $p_T > 0.5$ GeV/c. Authors also require $p_T(p) > p_T(\pi^+)$ to suppress Λ_c^+ combinatorial background. No particle identification is used in this analysis. All particle hypotheses consistent with the candidate decay structure are considered. In a 3D kinematic fit, the Λ_c^+ daughter

tracks are constrained to originate from a single point. The Λ_c^+ candidate is constrained to the known Λ_c^+ mass, and the Λ_c^+ momentum vector is extrapolated to intersect the π^- momentum vector to form the Λ_b^0 vertex. The probability of the 3D Λ_b^0 kinematic vertex fit must exceed 0.1%, and the Λ_c^+ and Λ_b^0 must have p_T greater than 4.5 and 6.0 GeV/c, respectively. To suppress prompt backgrounds from the primary interaction, the following decay-time requirements were made: $ct(\Lambda_b^0) > 250$ μm and its significance $ct(\Lambda_b^0)/\sigma_{ct} > 10$. It was defined $ct(\Lambda_b^0) \equiv L_{xy}(\Lambda_b^0)m_{\Lambda_b^0}c/p_T(\Lambda_b^0)$ as the Λ_b^0 proper time, where $L_{xy}(\Lambda_b^0)$ is defined as the projection onto $p_T(\Lambda_b^0)$ of the vector connecting the primary vertex to the vertex in the transverse plane. There was used a primary vertex determined event by event when computing this vertex displacement. To reduce combinatorial backgrounds and partially reconstructed decays, it was also required $|d_0(\Lambda_b^0)| < 80$ μm, where d_0 (Λ_b^0) is the impact parameter of the momentum vector of the Λ_b^0 candidate with respect to the primary vertex. To suppress the contributions from $B^0 \to D^+\pi^-$ decays, where $D^+ \to K^-\pi^+\pi^+$, it was required $m(pK^-\pi^+)$ to be within 16 MeV/c^2 of the known Λ_c^+ mass [79] and $ct(\Lambda_c^+) \in |-70, 200|$ μm. It was also defined $ct(\Lambda_c^+) \equiv L_{xy}(\Lambda_c^+)m_{\Lambda_c^+}c/p_T(\Lambda_c^+)$ as the Λ_c^+ proper time, where $L_{xy}(\Lambda_c^+)$ is defined analogously to $L_{xy}(\Lambda_b^0)$ but computed with respect to the Λ_b^0 vertex.

The invariant mass distribution of $\Lambda_c^+\pi^-$ candidates is shown in Fig. 17 overlaid with a binned maximum likelihood fit. A clear $\Lambda_b^0 \to \Lambda_c^+\pi^-$ signal is
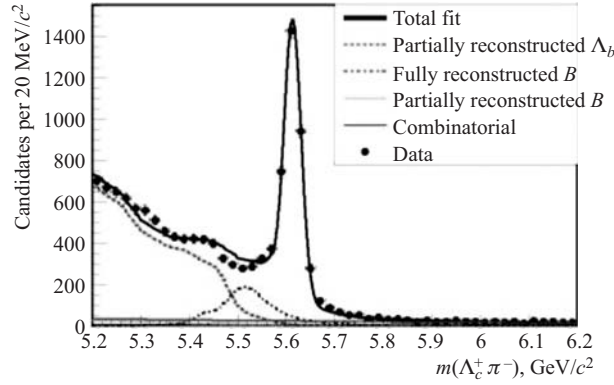
Fig. 17. Fit to the invariant mass of $\Lambda_b^0 \to \Lambda_c^+\pi^-$ candidates. Curves for fully reconstructed Λ_b^0 decays such as $\Lambda_b^0 \to \Lambda_c^+\pi^-$ and $\Lambda_b^0 \to \Lambda_c^+K^-$ are not indicated in the figure. The Λ_b^0 signal region, $m(\Lambda_c^+\pi^-) \in |5.565, 5.670|$ consists primarily of Λ_b^0 baryons, with some contamination from B mesons and combinatorial events. The discrepancies between the fit and data below the Λ_b^0 signal region are due to incomplete knowledge of the branching ratios of the decays in this region and are included in the $\Sigma_b^{(*)}$ background model systematics

observed at the expected Λ_b^0 mass. The invariant mass distribution is described by several components: the $\Lambda_b^0 \to \Lambda_c^+ \pi^-$ signal, a combinatorial background, partially and fully reconstructed B mesons which pass the $\Lambda_c^+ \pi^-$ selection criteria, partially reconstructed Λ_b^0 decays, and fully reconstructed Λ_b^0 decays other than $\Lambda_c^+ \pi^-$ (e.g., $\Lambda_b^0 \to \Lambda_c^+ K^-$). The combinatorial background is modeled with an exponentially decreasing function. All other components are represented in the fit by fixed shapes derived from Monte Carlo (MC) simulations* [90]. The normalizations are constrained by Gaussian terms to branching ratios that are either measured (for B-meson decays) or theoretically predicted (for Λ_b^0 decays). In the fit, the Λ_b^0 components are normalized relative to the $\Lambda_b^0 \to \Lambda_c^+ \pi^-$ signal. To normalize the B-meson components, there was explicitly reconstructed a $\bar{B}^0 \to (K^- \pi^+ \pi^+) \pi^-$ signal in the $\Lambda_c^+ \pi^-$ sample by replacing the proton-mass hypothesis with the pion-mass hypothesis. The fit to the invariant $\Lambda_c^+ \pi^-$ mass distribution results in $3180 \pm 60(\text{stat.})$ $\Lambda_b^0 \to \Lambda_c^+ \pi^-$ candidates.

The reconstruction of $\Sigma_b^{(*)}$ proceeds by combining Λ_b^0 candidates in the Λ_b^0 signal region, $m(\Lambda_c^+ \pi^-) \in [5.565, 5.670]$ GeV/c^2, with all remaining high quality tracks. A pion mass hypothesis is used when computing the invariant mass of the $\Sigma_b^{(*)}$ candidate. Search for narrow resonances was carried out in the mass difference distribution of $Q = m(\Lambda_b^0 \pi) - m(\Lambda_b^0) - m(\pi)$, where $m(\Lambda_b^0)$ is the reconstructed $\Lambda_c^+ \pi^-$ mass. The $\Sigma_b^{(*)}$ candidates are divided into two subsamples using the charge of the pion from $\Sigma_b^{(*)}$ decay, denoted by π_{Σ_b}: in the $\Lambda_b^0 \pi^-$ subsample the π_{Σ_b} has the same charge as the pion from Λ_b^0, while in the $\Lambda_b^0 \pi^+$ subsample the π_{Σ_b} has the opposite charge as the pion from Λ_b^0.

The $\Sigma_b^{(*)}$ signal region, defined as $Q \in [30, 100]$ MeV/c^2, is motivated by the predictions in [83–87]. The signal is modeled by the PYTHIA [55] event generator where only the decays $\Sigma_b^{(*)} \to \Lambda_b^0 \pi$, $\Lambda_b^0 \to \Lambda_c^+ \pi^-$, and $\Lambda_c^+ \to p K^- \pi^+$ are allowed. The $\Sigma_b^{(*)}$ selection criteria were optimized by maximizing $\varepsilon(S_{\text{MC}})/\sqrt{B}$, where $\varepsilon(S_{\text{MC}})$ is the efficiency of the $\Sigma_b^{(*)}$ signal measured in the MC simulation and B is the number of background events in the signal region estimated from the upper and lower sideband regions of $Q \in [0, 30]$ MeV/c^2 and $Q \in [100, 500]$ MeV/c^2. These sideband regions are parameterized by a power law multiplied by an exponential. The $\Lambda_b^0 \pi^-$ and $\Lambda_b^0 \pi^+$ subsamples were combined to optimize cuts on p_T of the $\Sigma_b^{(*)}$ candidate, the impact parameter significance $|d_0/\sigma_{d_0}|$ of the π_{Σ_b} track, and $\cos \theta^*$ of the π_{Σ_b} track, where θ^* is defined as the angle between the momentum of π_{Σ_b} in the $\Sigma_b^{(*)}$ rest frame and the direction

---

*There is used a variety of single b-hadron simulations; all using the $p_T(B)$ and $y(B)$ distributions obtained from B decays in data. The simulated $p_T(\Lambda_b^0)$ distribution is reweighted to match the sideband-subtracted data.

of the total $\Sigma_b^{(*)}$ momentum in the lab frame. The maximum of $\varepsilon(S_{\mathrm{MC}})/\sqrt{B}$ is realized for $p_T(\Sigma_b) > 9.5$ GeV/c, $|d_0/\sigma_{d_0}| < 3.0$, and $\cos\theta^* > -0.35$.

In the $\Sigma_b^{(*)}$ search, the dominant background is from the combination of prompt Λ_b^0 baryons with extra tracks produced in the hadronization of the b quark. The remaining backgrounds are from the combination of hadronization tracks with B mesons reconstructed as Λ_b^0 baryons, and from combinatorial background events. The percentage of each background component in the Λ_b^0 signal region, computed from the Λ_b^0 mass fit, is $(89.5 \pm 1.7)\%$ Λ_b^0 baryons, $(7.2 \pm 0.6)\%$ B mesons, and $(3.3 \pm 0.1)\%$ combinatorial events. Other backgrounds such as 5-track decays of B^+ mesons are negligible, as confirmed in inclusive single b-hadron simulations [90]. The high-mass region above the $\Lambda_b^0 \to \Lambda_c^+ \pi^-$ signal in Fig. 17 determines the combinatorial background shape. Reconstructing $\bar{B}^0 \to D^+ \pi^-$ data as $\Lambda_b^0 \to \Lambda_c^+ \pi^-$ gives the B hadronization background shape. The Λ_b^0 hadronization background shape is obtained from a $\Lambda_b^0 \to \Lambda_c^+ \pi^-$ PYTHIA simulation. The events in this simulation are reweighted so that the $p_T(\Lambda_b^0)$ distribution agrees with data. The background shapes are parameterized by a power law multiplied by an exponential, and the normalizations are fixed from the percentage of that background component in the Λ_b^0 signal region. The total background shown in Fig. 18 (insets) is compatible with the Q sidebands, and the background shape and normalization are fixed components of the $\Sigma_b^{(*)}$ fit. In the Q signal region there was observed an excess of events over the total background as shown in Fig. 18. The excess in the $\Lambda_b^0 \pi^-$ subsample is 118 over 288 expected background candidates. In the $\Lambda_b^0 \pi^+$ subsample the excess is 91 over 313 expected background candidates.

Authors perform a simultaneous unbinned maximum likelihood fit to the $\Lambda_b^0 \pi^-$ and $\Lambda_b^0 \pi^+$ subsamples for a signal from each expected $\Sigma_b^{(*)}$ state plus the background, referred to as the «four-signal hypothesis». Each signal consists of a nonrelativistic Breit–Wigner distribution convoluted with two Gaussian distributions describing the detector resolution, with a dominant narrow core of a 1.2 MeV/c^2 width and a small broad component of a 3 MeV/c^2 width for the tails. The natural width of each Breit–Wigner distribution is computed from the central Q value [89]. The expected difference of the isospin mass splittings within the Σ_b^* and Σ_b multiplets is below sensitivity with this sample of data. Consequently, $m(\Sigma_b^{*+}) - m(\Sigma_b^+) = m(\Sigma_b^{*-}) - m(\Sigma_b^-) \equiv \Delta_{\Sigma_b^*}$ was constrained. The four Σ_b signal fit to data, which has a fit probability of 76% in the range $Q \in |0, 200|$ MeV/c^2, is shown in Fig. 18.

Systematic uncertainties on the mass difference and yield measurements fall into three categories: mass scale, $\Sigma_b^{(*)}$ background model, and $\Sigma_b^{(*)}$ signal parameterization. The systematic uncertainty on the mass scale is determined by the discrepancies of the CDF II measured Q values of the D^*, Σ_c, and Λ_c^* hadrons from the world average Q values [79]. The Q-value dependence of
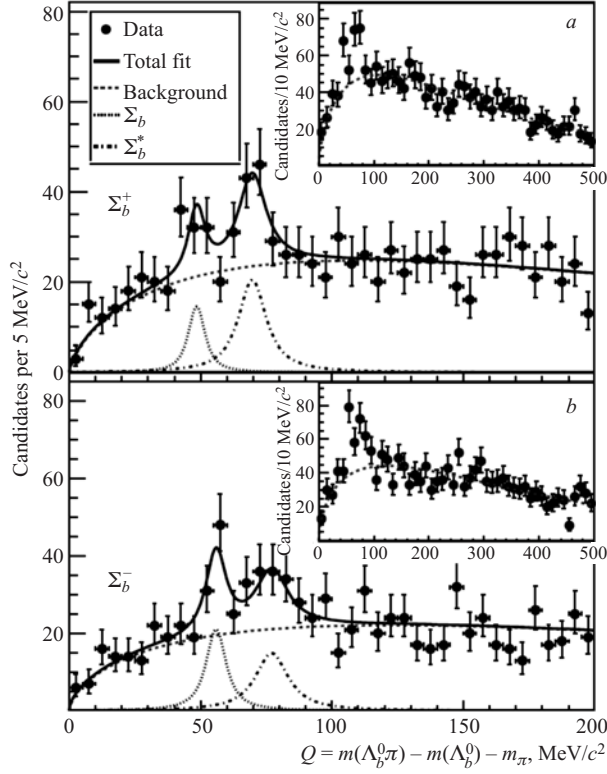
Fig. 18. The $\Sigma_b^{(*)}$ fit of the $\Lambda_b^0\pi^+$ and $\Lambda_b^0\pi^-$ subsamples. The plot a shows the $\Lambda_b^0\pi^+$ subsample, which contains $\Sigma_b^{(*)+}$, while the plot b shows the $\Lambda_b^0\pi^-$ subsample, which contains $\Sigma_b^{(*)-}$. The insets show the expected background plotted on the data for $Q \in |0, 500|$ MeV/c^2, while the signal fit is shown on a reduced range of $Q \in |0, 200|$ MeV/c^2

this systematic uncertainty is modeled with a linear function, which is used to extrapolate the mass scale uncertainty for each $\Sigma_b^{(*)}$ Q value. This is the largest systematic uncertainty for the mass difference measurements, ranging from 0.1 to 0.3 MeV/c^2. The systematic effects related to assumptions made on the $\Sigma_b^{(*)}$ background model are: the sample composition of the Λ_b^0 signal region, the normalization and functional form of the Λ_b^0 hadronization background taken from a PYTHIA simulation, and limited knowledge of the shape of the Λ_b^0 hadronization background (the largest systematic uncertainty on the yield measurements, ranging from 2 to 15 events). The systematic effects related to assumptions made on the $\Sigma_b^{(*)}$ signal parameterization are: underestimation of the detector resolu-

tion, the uncertainty in the natural width prediction from [89], and the constraint $m(\Sigma_b^{*+}) - m(\Sigma_b^+) = m(\Sigma_b^{*-}) - m(\Sigma_b^-)$.

The significance of the signal is evaluated using the likelihood ratio, $LR = L/L_{\mathrm{alt}}$, where L is the likelihood of the four-signal hypothesis and L_{alt} is the likelihood of an alternative hypothesis [91]. The alternate hypotheses of no signal were studied, two Σ_b states (one per $\Lambda_b^0 \pi$ charge combination), and three $\Sigma_b^{(*)}$ states, performed by eliminating one of the states in the four-signal hypothesis. The resulting likelihood ratios are given in Table 9. To assess the significance of the signal, the four-signal hypothesis fit was repeated on samples randomly generated from alternate signal hypotheses. In 12 million background samples, none had an LR equivalent or greater than the one found in data. There was evaluated the probability for background only to produce four signals of this or greater significance to be less than $8.3 \cdot 10^{-8}$ corresponding to a significance of greater than 5.2σ. The probabilities for each of the alternate hypotheses are also given in Table 9. The final results for the Σ_b measurement are quoted in Table 10. Using the CDF II measurement of $m(\Lambda_b^0) = (5619.7 \pm 1.2(\mathrm{stat.}) \pm$

Table 9. **Likelihood ratios (*LR*) in favor of the four-signal hypothesis over alternative hypotheses. Also shown is the probability for each hypothesis to produce the observed data (*p* value), calculated using the *LR* as a test statistic on randomly generated samples. The final column gives the equivalent standard deviations from the normal distribution**

Hypothesis	LR	p value	Significance (σ)
No Signal	$2.6 \cdot 10^{18}$	$< 8.3 \cdot 10^{-8}, 9.2 \cdot 10^{-5}$	> 5.2
Two Σ_b states	$4.4 \cdot 10^6$	$9.2 \cdot 10^{-5}$	3.7
No Σ_b^- signal	$1.2 \cdot 10^5$	$3.2 \cdot 10^{-4}$	3.4
No Σ_b^+ signal	49	$9.0 \cdot 10^{-3}$	2.4
No Σ_b^{*-} signal	$4.9 \cdot 10^4$	$6.4 \cdot 10^{-4}$	3.2
No Σ_b^{*+} signal	$8.1 \cdot 10^4$	$6.0 \cdot 10^{-4}$	3.2

Table 10. **Final results for the Σ_b measurement. The first uncertainty is statistical and the second is systematic. The absolute Σ_b mass values are calculated using a CDF II measurement of the Λ_b^0 mass [78], which contributes to the systematic uncertainty**

State	Yield	Q or $\Delta_{\Sigma_b^*}$, MeV/c^2	Mass, MeV/c^2
Σ_b^+	32^{+13+5}_{-12-3}	$Q_{\Sigma_b^+} = 48.5^{+2.0+0.2}_{-2.2-0.3}$	$5807.8^{+2.0}_{-2.2} \pm 1.7$
Σ_b^-	59^{+15+9}_{-14-4}	$Q_{\Sigma_b^-} = 55.9 \pm 1.0 \pm 0.2$	$5815 \pm 1.0 \pm 1.7$
Σ_b^{*+}	77^{+17+10}_{-16-6}		$5829.0^{+1.6+1.7}_{-1.8-1.8}$
		$\Delta Q_{\Sigma_b^*} = 21.2^{+2.0+0.4}_{-1.9-0.3}$	
Σ_b^{*-}	69^{+18+16}_{-17-5}		$5836.4 \pm 2.0^{+1.8}_{-1.7}$

1.2(syst.)) MeV/c^2 [78], the absolute masses of the Σ_b states given in Table 10 were found. The systematic uncertainties on the absolute Σ_b mass values are dominated by the total Λ_b^0 mass uncertainty.

In summary, using a sample of 3180 ± 60(stat.) $\Lambda_c^+\pi^-$ candidates reconstructed in 1.1 fb^{-1} of CDF II data, there was realized search for resonant $\Lambda_b^0\pi^\pm$ states. Authors observe a signal of four states, whose masses and widths are consistent with those expected for the lowest-lying charged $\Sigma_b^{(*)}$ baryons. This result represents the first observation of the Σ_b and Σ_b^* baryons.

3.4. Observation and Mass Measurement of the Baryon Ξ_b^-. From the very beginning the quark model has had great success in describing the spectroscopy of hadrons. It has been successful for the B mesons, where all of the ground states have been observed. A rich spectrum of baryons containing b quarks was also predicted [84, 85, 87, 88]. However, direct observation of b baryons has been limited to a single state, Λ_b (content udb) until $\sim$1995. Evidence for b baryons that also contain a strange quark was shown from LEP [92] through partial reconstruction of decays containing electrons and muons. The mix of Ξ_b^- (quark content dsb) and Ξ_b^0 (quark content usb) was measured by DELPHI (1995, 2005) and ALEPH (1996) collaborations. Ξ_b mass could not be measured in these experiments because only semileptonic decays were studied. Recent results from the Tevatron on the Σ_b states [81] and Ξ_b^- [93, 94] are beginning to closer examination of b baryons.

In 2007, D$\emptyset$ [93] has made the direct observation of Ξ_b^- in the decay channel $\Xi_b^- \to J/\psi\Xi^-$ and has measured its mass: $(5774\pm11\pm15)$ MeV/c^2. At the same time, CDF II collaboration has obtained more precise and statistically significant value of Ξ_b^- mass equal to: $(5792.9 \pm 2.5(\text{stat.}) \pm 1.7(\text{syst.}))$ MeV/c^2 [94]. This observation is made through the decay chain $\Xi_b^- \to J/\psi\Xi^-$, where $J/\psi \to \mu^+\mu^-$, $\Xi^- \to \Lambda\pi^-$, and $\Lambda \to p\pi^-$. (Charge conjugate modes are included implicitly.) The CDF measurement is based on a data sample with an integrated luminosity of 1.9 fb^{-1}.

The analysis of the data begins with a selection of well-measured $J/\psi \to \mu^+\mu^-$ candidates. The trigger requirements are confirmed by selecting events that contain two oppositely charged muon candidates, each with matching COT and muon chamber tracks. The central muon chambers cover the pseudorapidity region $|\eta| < 0.6$, and are sensitive to muons with transverse momentum $p_T > 1.4$ GeV/c. A second muon system covers the region $0.6 < |\eta| < 1.0$ and detects muons having $p_T > 2.0$ GeV/c. There is also requirement that both muon tracks have associated measurements in at least three layers of the silicon detector and a two-track invariant mass within 80 MeV/c^2 of the world-average J/ψ mass 3097 MeV/c^2 [79]. This data sample provides approximately 15 million events containing J/ψ candidates, measured with an average mass resolution of 20 MeV/c^2. The majority of Ξ^- candidates have $p_T > 1.5$ GeV/c. This,

along with the long lifetime of Ξ^- ($c\tau = 4.9$ cm) [79], results in a significant fraction of the Ξ^- candidates having decay vertices located several centimeters radially outward from the beam line. That helps in doing refined fit (see below).

The reconstruction of Ξ^- candidates uses all additional tracks found in each selected J/ψ event. Pairs of oppositely charged tracks are used to identify Λ decay. The proton (pion) mass is assigned to the track with the higher (lower) momentum. This mass assignment is always correct for $\Lambda \rightarrow p\pi^-$ candidates used in this analysis because of the kinematics of Λ decay with the lower limit of ≈ 200 MeV/c in the transverse momentum acceptance of the tracking system. The Λ mass is measured with a resolution of 2.5 MeV/c^2. All intersecting pairs of tracks with an invariant mass within 10 MeV/c^2 of the world-average Λ mass 1115.7 MeV/c^2 [79] have their track parameters recalculated according to a fit to the Λ mass. The decay vertex is used to calculate the Λ displacement from the beam line in the direction of the track pair's transverse momentum. The background due to tracks originating from the primary vertex is reduced by requiring this displacement to exceed 1.0 cm. For candidates that satisfy these requirements, the remaining tracks are assigned the pion mass, and $\Lambda\pi^-$ combinations are identified that are consistent with the decay process $\Xi^- \rightarrow \Lambda\pi^-$. In order to obtain the best possible $\Lambda\pi^-$ mass resolution, the reconstruction uses a fit on the three tracks that simultaneously constrains the Λ decay products to the Λ mass, and the Λ trajectory to intersect with the helix of the decay pion. For all Ξ^- candidates, the reconstructed decay position of the Λ candidate is required to be radially displaced at least 1.0 cm with respect to the reconstructed decay vertex of the Ξ^- candidate.

As it has been told above, the majority of Ξ^- candidates having decay vertices are displaced several centimeters radially outward from the beam line. Therefore, it is possible to refine the Ξ^- reconstruction by making use of the improved determination of the trajectory that can be obtained by tracking Ξ^- in the silicon detector. The Ξ^- candidates have an additional fit performed on the three tracks that simultaneously constrains both the Λ and Ξ^- masses of the appropriate track combinations, and provides the best possible estimate of the Ξ^- momentum and decay position. The result of this fit is used to define a helix that serves as the seed for an algorithm that searches for silicon detector hits associated with the Ξ^- track. Further analysis of all Ξ^- candidates consists of measurements in at least two layers of the silicon detector. This technique provides excellent impact parameter resolution for the Ξ^- track (average of 60 μm), and has been used previously [95]. The $\Lambda\pi^-$-invariant mass spectrum of all combinations that satisfy these requirements is shown in Fig. 19. Approximately 23,500 Ξ^- candidates above the combinatorial background are identified. The Ξ_b^- search includes the subset of these combinations with an invariant mass within 10 MeV/c^2 of the world-average Ξ^- mass [79].
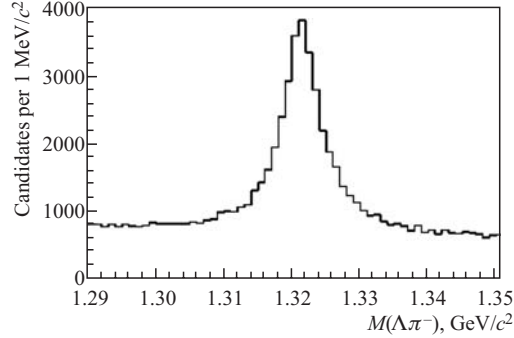
Fig. 19. The invariant mass distribution of $\Lambda\pi^-$ combinations having an associated track in the silicon detector in events containing J/ψ candidates

A Monte Carlo simulation that generates b quarks according to a next-to-leading-order calculation [96], allows one to receive the mass resolution for the J/ψ final state and produces Ξ_b^- events by simulating b-quark fragmentation [97]. The decay $\Xi_b^- \to J/\psi\Xi^-$ is simulated with EvtGen [90]. The generated events are used as input to the detector and trigger simulations based on a GEANT3 description [98] and processed through the same reconstruction and analysis algorithms used for the data. Analysis of the simulated Ξ_b^- events shows that a 10% improvement in mass resolution can be obtained if the momenta of the Ξ_b^- decay products are allowed to vary in the fit of the Ξ_b^- candidate, rather than simply using the Ξ^- track. Consequently, a procedure that simultaneously fits the five tracks of the final state, constrains the three vertices of the decay chain to the appropriate topology, and constrains the masses of J/ψ, Ξ^-, and Λ to their world-average masses [79], is used to provide the best estimate of the $J/\psi\ \Xi^-$ mass. The average Ξ_b^- mass resolution obtained from simulated events is found to be approximately 15 MeV/c^2. It was also noted that the $J/\psi\Xi^-$ invariant mass resolution is comparable to the mass resolution obtained with the CDF II detector for other B hadrons with a J/ψ in the final state.

The selection used to single out the $\Xi_b^- \to J/\psi\Xi^-$ decay process is guided by the properties of other B hadrons that include a J/ψ in the final state. The very important ones include the lifetime of the ground-state B hadrons and the energy available in the decay. The $B^{\pm}, B^0$ and B_S mesons and Λ_b baryon all have lifetimes dominated by the weak decay of the b quark. One can expect the same to hold true for Ξ_b^- and for its lifetime to be comparable to these states. One expects the energy released in the decay of Ξ_b^- to be comparable. This expectation is also consistent with the range of theoretical predictions (5788–5812 MeV/c^2) for the Ξ_b^- mass [84, 85, 87, 88].

Authors [94] developed the event selection method by which $B^{\pm} \to J/\psi K^{\pm}$ decays were studied. This final state is identified by assigning the $K^{\pm}$ mass to all tracks not used in the J/ψ reconstruction. Each three-track combination must satisfy a fit where the tracks are required to originate from a common vertex and the invariant mass of the muon pair is constrained to the world-average J/ψ mass [79]. Approximately 30,000 $B^{\pm}$ candidates are identified in this sample. Several characteristics of the final state are used as selection requirements to obtain a $B^{\pm}$ signal with very little background. Minimum transverse momentum requirements on the $K^{\pm}$ and $B^{\pm}$ candidates are used to suppress backgrounds from the event that are not related to the $B^{\pm}$ decay. The trajectory of $K^{\pm}$ is required to originate from the $B^{\pm}$-decay vertex by placing a requirement on its impact parameter $d_{\mathrm{SV}}(K)$ and associated uncertainty $\sigma_{d_{\mathrm{SV}}}(K)$ with respect to the vertex found in the J/ψ fit. Similar impact parameter quantities $d_{\mathrm{PV}}(K)$ and $\sigma_{d_{\mathrm{PV}}}(K)$ measured with respect to the primary vertex are used to remove tracks that originate from the prompt background. Reasonable vertex quality is assured by placing a minimum value on the accepted probability $P(\chi^2)$ of the mass- and vertex-constrained fit used to obtain the $B^{\pm}$ candidate. If one suppresses the promptly-produced combinatorial background by rejecting candidates with low proper decay time, $t \equiv \bar{L}_T \times \bar{p}_T(B) M(B)/|p_T(B)|^2$, where $M(B)$ is the mass of the $B^{\pm}$ candidate, $\bar{p}_T(B)$ is the transverse momentum of the $B^{\pm}$ candidate, and $\bar{L}_T$ is the transverse displacement of the $B^{\pm}$-decay vertex from the beam line. A requirement on proper decay time uncertainty σ_t removes poorly-reconstructed combinations. There were also rejected combinations that are inconsistent with having originated from the beam line by requiring a small magnitude of the impact of the $B^{\pm}$ candidate, $\bar{d}_{\mathrm{PV}}(B) \equiv \bar{L}_T \times p_T(B)/|p_T(B)|$, and a small angle β between $\bar{L}_T$ and $p_T(B)$.

This analysis uses a two-step selection procedure. Final selection criteria are listed in Table 11. Authors [94] first impose the «standard» selection requirements listed there and retain all $J/\psi K^{\pm}$ combinations that satisfy them. Any combination that fails only one of the «standard» selection requirements is also allowed into the final sample if it satisfies both of the p_T requirements of the «high-p_T» selection requirements and fails no more than one of other requirements in this set. The combination of «standard» and «high-p_T» requirements reduces the background in the $B^{\pm} \to J/\psi K^{\pm}$ sample to approximately 400 combinations, while retaining a signal of 16,000 $B^{\pm}$ candidates.

As is done for the reconstruction of $B^{\pm}$, the treatment of the $J/\psi \Xi^-$ candidates requires a mass- and vertex-constrained fit on the muon candidates and the Ξ^- track. The selection criteria in Table 11 are applied to the $J/\psi \Xi^-$ sample, where simply were exchanged K^- for Ξ^- and $B^{\pm}$ for Ξ_b^- where appropriate. Combinations that satisfy these requirements form the final set of Ξ_b^- candidates. The invariant mass of each candidate is obtained with the full five-track fit, and the resulting $J/\psi \Xi^-$ mass distribution is shown in Fig. 20.

Table 11. **Selection variables and requirements for the «standard» selection and «high-p_T» selection as described in the text**

Selection variable	Standard	High-p_T
$p_T(K)$, GeV/c	> 1.7	> 2.5
$p_T(B)$, GeV/c	> 5	> 6
$|d_{\mathrm{SV}}(K)|$, μm	< 100	< 80
$|d_{\mathrm{PV}}(K)|/\sigma_{d_{\mathrm{PV}}(K)}$	> 2.5	> 3
$|d_{\mathrm{PV}}(B)|$, μm	< 75	< 60
ct, μm	> 80	> 100
$c\sigma_t$, μm	< 30	< 25
$P(\chi^2)$, %	> 0.1	> 1
β, rad	< 0.4	< 0.3

Note. Here K refers to the third track combined with J/ψ and is a $K^\pm$ or Ξ^- candidate for the $B^\pm$ or Ξ_b^- candidates, respectively. Similarly, B refers to either $B^\pm$ or Ξ_b^-, as is appropriately chosen Ξ_b^- search strategy that will provide an optimal sensitivity for a final state that shares similar properties with these well-established B hadrons.
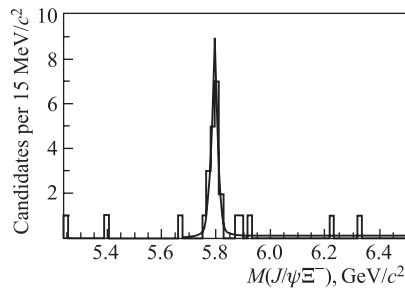

Fig. 20. The $J/\psi\Xi^-$ invariant mass distribution for combinations that satisfy the selection requirements. The projection of the fit function is overlaid on the data

The mass resolution estimate for Ξ_b^- implies that more than 95% of a Ξ_b^- signal will occupy an invariant-mass bin with a width of 75 MeV/c^2. The data shown in Fig. 20 contain 18 candidates in the 75 MeV/c^2 range of 5750–5825 MeV/c^2. Authors model the combinatorial background by considering candidates in the range 5700–6500 MeV/c^2; the data yield 23 candidates in this range. No events contribute multiple candidates. The upper limit of this range is chosen arbitrarily, and has no impact on the result. The lower limit is chosen to avoid partially reconstructed $\Xi_b^{-,0} \to J/\psi\Xi^- X$ decays, where X represents additional undetected particles. It was assumed that the mass distribution of the combinatorial background is uniform and that the occupancy due to background combinations in any particular 75 MeV/c^2 mass bin within the 800 MeV/c^2 search range can be described by a binomial distribution, with a

single-event probability given by the ratio of the two mass ranges used. The probability that the number of candidates observed in the 5750–5825 MeV/c^2 mass range is due to a background fluctuation is estimated as the binomial probability of 18 or more events from a sample of 23 total occurrences and a single-event probability of 75/800. This probability is $6.6 \cdot 10^{-15}$, equivalent to a 7.7σ variation from a Gaussian distribution. Consequently, authors [94] interpret the data distribution shown in Fig. 20 to be the observation of a resonance, with a width consistent with the detector resolution. Comparable distributions of $J/\psi \Lambda \pi^+$ and $J/\psi \Lambda \pi^-$, where $\Lambda \pi^-$ does not form a Ξ^-, yield no significant enhancement at any mass within the range of this analysis.

   The masses and their uncertainties obtained from the five-track final-state fit method are used in an unbinned likelihood fit to measure the Ξ_b^- mass. The negative log-likelihood function that is minimized has the form:

$$L = -2 \sum_{i=1}^{N} \ln[fG(m_i, m_0, s_m \sigma_i^m) + (1 - f)C], \qquad (6)$$

where m_i is the mass obtained for a single candidate; σ_i^m is the uncertainty on that mass as estimated from the track parameters for the candidate; $G(m_i, m_0, s_m \sigma_i^m)$ is a Gaussian distribution with average m_0 and characteristic width $s_m \sigma_i^m$, and C is a constant background term. The quantities obtained from the fitting procedure include f, the fraction of the events found in the signal, m_0, the best average mass, and s_m, a scale factor on the mass uncertainty which accounts for a possible shift in the mass uncertainty. This procedure yields a best estimate for the Ξ_b^- mass of (5792.9 ± 2.5) MeV/c^2. The uncertainty scale factor is determined to be 2.0 ± 0.4, which is consistent with the value of 1.6 ± 0.2 obtained with simulated Ξ_b^- candidates. The signal fraction is calculated to be 0.76 ± 0.09, giving a yield of (17.5 ± 4.3) Ξ_b^- candidates in this data sample. The projection of the fit function is superimposed in Fig. 20.

   Several systematic effects have been considered for their impact on the Ξ_b^- mass measurement. The overall momentum scale of the tracking system is established by calibrating with the well-measured J/ψ, $\psi(2S)$, and Y states [78]. The momentum scale uncertainty contributes a systematic established uncertainty of ± 0.4 MeV/c^2 on the Ξ_b^- mass measurement. Alignment and material distribution of the tracking system contributes an additional ± 0.6 MeV/c^2 of uncertainty. The method requires knowledge of the mass of the final state Ξ^-, a quantity that is known to ± 0.13 MeV/c^2 [79]. The mass uncertainty of J/ψ is included in the momentum scale calibration, and the mass uncertainty of Λ (± 0.006 MeV/c^2) is negligible for this analysis. Finally, the largest systematic variation seen on the mass measurement occurs when alternative fitting models are used for the mass calculation. The signal distribution has been fit with a single Gaussian, where its parameters are allowed to vary in the fit. A double Gaussian is also used,

where the widths are fixed to values obtained in simulation, and only the average mass is allowed to vary. These different models for the probability distribution function of the signal create variations of ± 1.5 MeV/c^2 on the mass result. The individual systematic uncertainties are combined in quadrature to obtain an overall systematic uncertainty of ± 1.7 MeV/c^2 on the Ξ_b^- mass measurement.

In outcome, Ξ_b^- has been observed with the CDF II detector in $p\bar{p}$ collisions at 1.96 TeV. A signal with (17.5 ± 4.3) Ξ_b^- candidates and a significance of 7.7σ is seen in the decay channel $\Xi_b^- \rightarrow J/\psi \Xi^-$, the mass of this baryon is measured to be $(5792.9 \pm 2.5(\text{stat.}) \pm 1.7(\text{syst.}))$ MeV/c^2, which is consistent with theoretical expectations [84, 85, 87, 88]. The mass measurement presented is also consistent with the only other direct observation of this state [93], and represents a significant improvement in precision.

CONCLUSION

The considered physical results are mainly those that CDF collaboration calls «discovery» (http://www-cdf.fnal.gov/physics/highlights.html). As one can see, the CDF II detector is able to fulfill quite different tasks at the very high science and statistical level. Let us stress here that a CDF/JINR group created significant contribution to the new CDF Complex and physical investigation. There are certainly other wonderful publications made on the base of statistical material collected with help of CDF detector that could be included in such a review, many of them deserve separate consideration. Among them are: search for Higgs & Exotics, world's most precise W-boson mass determination, evidence for single top production, evidence for $D^0 - \bar{D}^0$ mixing and many others. But it is impossible to come over immensity in this review. Let us leave them for the next time.

REFERENCES

1. *Abe F. et al. (CDF Collab.).* Observation of Top-Quark Production in $p\bar{p}$ Collisions with the Collider Detector at Fermilab // Phys. Rev. Lett. 1995. V. 74. P. 2626; *Abachi S. et al. (D∅ Collab.).* Observation of the Top Quark // Ibid. P. 2632.

2. *CDF Collab., D∅ Collab., the Tevatron Electroweak Working Group.* Combination of CDF and D Results on the Top-Quark Mass. hep-ex/0404010.

3. *Miransky V. A., Tanabashi M., Yamawaki K.* Is the T Quark Responsible for the Mass of W and Z Bosons? // Mod. Phys. Lett. A. 1989. V. 4. P. 1043.

4. *Altarelli G., Grunewald M. W.* Precision Electroweak Tests of the Standard Model // Phys. Rev. 2004. V. 403–404. P. 189201;
Xiao Z. J. et al. Implications of the Top-Quark Mass Measurement for the SM Higgs Boson Mass $M(H)$ // J. Phys. G. 1995. V. 21. P. 19.

5. *Bellettini G. et al. (CDF Collab.).* Measurement of the Top-Quark Mass Using the MINUIT Fitter in Dilepton Events at CDF. JINR, E1-2005-18. Dubna, 2005. P. 12.

6. *Bellettini G. et al. (CDF Collab.).* Top-Quark Mass Measurement in Non-Tagged Lepton + Jets Events at CDF. FERMILAB-pub-05-565-e; JINR, E1-2005-17. Dubna, 2005. P. 8.

7. *Bellettini G. et al. (CDF Collab.).* Measurement of the Top-Quark Mass Using Neurino Phi Weighting Method in Dilepton Events at CDF. JINR, E1-2005-129. Dubna, 2005. P. 12.

8. *Acosta D. et al. (CDF Collab.).* Top-Quark Mass Measurements Using the Template Method in the Lepton + Jets Channel at CDF II // Phys. Rev. D. 2006. V. 73. P. 032003.

9. *Budagov J. et al.* Review of the Top-Quark Mass Measurement at the CDF // Part. Nucl. 2007. V. 38. P. 734–770.

10. *Abulencia A. et al. (CDF Collab.).* Measurement of the Top-Quark Mass with the Dynamical Likelihood Method Using Lepton Plus Jets Events with b Tags in $p\bar{p}$ Collisions at $\sqrt{s} = 1.96$ TeV // Phys. Rev. D. 2006. V. 73. P. 092002.

11. The CDF II Detector Technical Design Report / Ed. Amidei D. Fermilab-Pub-96/390-E;
LeCompte T., Diehl H. T. The CDF and D∅ Upgrades for Run II // Ann. Rev. Nucl. Part. 2000. V. 50. P. 71–117.

12. *Sill A. (CDF Collab.).* CDF Run II Silicon Tracking Projects // Nucl. Instr. Meth. A. 2000. V. 447. P. 1.

13. *Affolder T. et al. (CDF Collab.).* CDF Central Outer Tracker // Nucl. Instr. Meth. A. 2004. V. 526. P. 249.

14. *Balka L. et al. (CDF Collab.).* The CDF Central Electromagnetic Calorimeter // Nucl. Instr. Meth. A. 1988. V. 267. P. 272.

15. *Gallinaro M. et al.* A New Scintillator Tile/Fiber Preshower Detector for the CDF Central Calorimeter // IEEE Trans. Nucl. Sci. 2005. V. 52. P. 879–883; e-PrintArch: physics. 0411056. 2004.

16. *Bertolucci S. et al. (CDF Collab.).* The CDF Central and Endwall Hadron Calorimeter // Nucl. Instr. Meth. A. 1988. V. 267. P. 301.

17. *Albrow M. G. et al. (CDF Collab.).* The CDF Plug Upgrade Electromagnetic Calorimeter: Test Beam Results // Nucl. Instr. Meth. A. 2002. V. 480. P. 524.

18. *Ascoli G. et al.* CDF Central Muon Detector // Nucl. Instr. Meth. A. 1988. V. 268. P. 33.

19. *Artikov A. M. et al.* Scintillation Counters of Muon System at CDF II // Part. Nucl. 2008. V. 39, No. 3. P. 410–423;
Artikov A. et al. Long Muon Scintillation Counters with Wavelength Shifter Fiber for CDF II // Part. Nucl., Lett. 2006. V. 3, No. 3(132). P. 81–102.

20. *Artikov A. et al.* Design and Construction of New Central and Forward Muon Counters for CDF II // Nucl. Instr. Meth. A. 2005. V. 538. P. 358–371.

21. *Artikov A. et al.* Properties of the Ukraine Polystyrene-Based Plastic Scintillator UPS 923A // Ibid. V. 555. P. 125–131.

22. *Pukhov O. et al.* Automatization of the Monitoring and Control of the Muon Scintillation Counters at CDF II // Part. Nucl., Lett. 2002. V. 5. P. 72–61.

23. *Thomson E. J. et al.* Online Track Processor for the CDF Upgrade // IEEE Trans. Nucl. Sci. 2002. V. 49, Iss. 3, Part 2. P. 1063–1070;
Acosta D. et al. The Performance of the CDF Luminosity Monitor // Nucl. Instr. Meth. A. 2002. V. 494. P. 57.

24. *Artikov A. et al.* Possible Modification of Level 1 Trigger of the CDF Muon System at Increased Tevatron Luminosity // Part. Nucl., Lett. 2008. V. 5, No. 2(144). P. 171–188.

25. *Battaiolo P. et al.* A Fast Track Finder for Triggering Applications in High-Energy Physics // Nucl. Instr. Meth. A. 1990. V. 293. P. 531–536.

26. *Boudreau J. (CDF Collab.).* What CDF Sees with Silicon Vertex Trigger // Mod. Phys. Lett. A. 2004. V. 19, No. 22. P. 1633–1648.

27. *Ashmanskas W. et al. (by CDF Collab.).* Silicon Vertex Tracker: A Fast Precise Tracking Trigger for CDF // Nucl. Instr. Meth. A. 2000. V. 447. P. 218–222.

28. *Ashmanskas W. et al. (by CDF Collab.).* The CDF Vertex Tracker: Online Precision Tracking of the CDF Detector // Nuovo Cim. A. 1999. V. 112. P. 1239–1243.

29. *Ashmanskas W. et al. (by CDF Collab.).* The CDF Silicon Vertex Tracker // Nucl. Instr. Meth. A. 2002. V. 477. P. 451–455.

30. *Ashmanskas W. et al.* The CDF Silicon Vertex Tracker: Tevatron RUN II Preliminary Results // Part. Nucl., Lett. 2002. No. 5[114]. P. 12–24.

31. *Ashmanskas W. et al.* Initial Experience with the CDF SVT Trigger // Nucl. Instr. Meth. A. 2003. V. 501. P. 201–206.

32. *Ashmanskas W. et al. (by CDF Collab.).* Trans Performance of the CDF Online Silicon Vertex Tracker // Nucl. Sci. 2002. V. 49. P. 1177–1184.

33. *Bardi A. et al.* The CDF Online Silicon Vertex Tracker // Nucl. Instr. Meth. A. 2002. V. 485. P. 178–182.

34. *Ashmanskas B. et al.* The CDF Silicon Vertex Trigger // Nucl. Instr. Meth. A. 2004. V. 518. P. 532–536.

35. *Abulencia A. et al.* Precision Measurement of the Top-Quark Mass from Dilepton Events at CDF II // Phys. Rev. D. 2007. V. 75. P. 031105(R).

36. *Kane G. L., Mrenna S.* Do about Half the Top Quarks at Fermilab Come from Gluino Decays? // Phys. Rev. Lett. 1996. V. 77. P. 3502.

37. *Abulencia A. et al. (CDF Collab.).* Top-Quark Mass Measurement from Dilepton Events at CDF II // Phys. Rev. Lett. 2006. V. 96. P. 152002.

38. *Abe F. et al. (CDF Collab.).* Measurement of the Top-Quark Mass with the Collider Detector at Fermilab // Phys. Rev. Lett. 1999. V. 82. P. 271.

39. *Abbot B. et al. (DØ Collab.).* Measurement of the Top-Quark Mass Using Dilepton Events // Phys. Rev. Lett. 1998. V. 80. P. 2063.

40. *Abulencia A. et al. (CDF Collab.).* Precision Top-Quark Mass Measurement in the Lepton + Jets Topology in $p\bar{p}$ Collisions at $\sqrt{s} = 1.96$ TeV // Phys. Rev. Lett. 2006. V. 96. P. 022004.

41. *Affolder T. et al. (CDF Collab.).* Measurement of the Top-Quark Mass with the Collider Detector at Fermilab // Phys. Rev. D. 2001. V. 63. P. 032003.

42. *Abazov V. et al. (DØ Collab.).* A Precision Measurement of the Mass of the Top Quark // Nature. 2004. V. 429. P. 638.

43. *Abazov V. et al. (DØ Collab.).* Measurement of the Top-Quark Mass in the Lepton Jets Final State with the Matrix Element Method // Phys. Rev. D. 2006. V. 74. P. 092005.

44. *Abulencia A. et al. (CDF Collab.).* Measurement of the Top-Quark Mass Using Template Methods on Dilepton Events in $p\bar{p}$ Collisions at $\sqrt{s} = 1.96$ TeV // Ibid. V. 73. P. 112006.

45. *Kondo K.* Dynamical Likelihood Method and Top-Quark Mass Measurement at CDF // J. Phys. Soc. Japan. 1988. V. 57. P. 4126.

46. *Goldstein G. et al.* Observing Top-Quark Production at the Fermilab Tevatron // Phys. Rev. D. 1993. V. 47. P. 967.

47. *Abulencia A. et al. (CDF Collab.).* Top Quark-Mass Measurement from Dilepton Events at CDF II with the Matrix Element Method // Phys. Rev. D. 2006. V. 74. P. 032009.

48. *Jayatilaka B.* A Measurement of the Top-Quark Mass in the Dilepton Decay Channel at CDF II. Ph. D. Thesis. Univ. Michigan, 2006.

49. *Acosta D. et al. (CDF Collab.).* Measurement of the tt Production Cross Section in $p\bar{p}$ Collisions at $\sqrt{s} = 1.96$ TeV Using Dilepton Events // Phys. Rev. Lett. 2004. V. 93. P. 142001.

50. *Corcella G. et al.* HERWIG 6: An Event Generator for Hadron Emission Reactions with Interfering Gluons (Including Supersymmetric Processes) // J. High Energy Phys. 2001. V. 01. P. 010.

51. *Affolder T. et al.* CDF II Detector Simulation // Nucl. Instr. Meth. A. 2000. V. 447. P. 1.

52. *Pumplin J. et al.* Global New Generation of Parton Distributions with Uncertainties from QCD Analysis // J. High Energy Phys. 2002. V. 07. P. 012.

53. *Mahlon G., Parke S.* Maximizing Spin Correlations in Top-Quark Pair Production at the Tevatron // Phys. Lett. B. 1997. V. 411. P. 173.

54. *Mangano M. L. et al.* ALPGEN, a Generator for Hard Multiparton Processes in Hadronic Collisions // J. High Energy Phys. 2003. V. 0307. P. 001; hep-ph/0206293.

55. *Sjostrand T. et al.* PYTHIA 6.2 Physics and Manual // Comp. Phys. Commun. 2001. V. 135. P. 238; hep-ph/0108264.

56. *Bhatti A. et al.* Probing QCD and New Probing QCD and New Physics with Jets at CDF // Nucl. Instr. Meth. A. 2006. V. 566. P. 375.

57. *Martin A. D. et al.* The α_S Dependence of Parton Distributions // Phys. Lett. B. 1995. V. 356. P. 89.

58. *Abulencia A. et al. (CDF Collab.).* Top-Quark Mass Measurement Using the Template Method in the Lepton Jets Channel at CDF II // Phys. Rev. D. 2006. V. 73. P. 32003.

59. *Aaltonen T. et al. (CDF Collab.).* Measurement of the Top-Quark Mass in All-Hadronic Decays in $p\bar{p}$ Collisions at CDF II // Phys. Rev. Lett. 2007. V. 98. P. 142001; hep-ex/0612026.

60. *The CDF Collab., the DØ Collab. and Tevatron Electroweak Working Group.* Tech. Rep. FERMILAB-TM-2355-E. Fermilab, 2006.

61. *Abulencia A. et al.* Precise Measurement of the Top-Quark Mass in the Lepton + Jets Topology at CDF II // Phys. Rev. Lett. 2007. V. 99. P. 182002.

62. *Acosta D. et al. (CDF Collab.).* Precision Top-Quark Mass Measurement in the Lepton + Jets Topology in $p\bar{p}$ Collisions at $\sqrt{s} = 1.96$ TeV // Phys. Rev. Lett. 2006. V. 96. P. 022004.

63. *Affolder T. et al. (CDF Collab.).* Measurement of the $t\bar{t}$ Production Cross Section in $p\bar{p}$ Collisions at $\sqrt{s} = 1.8$ TeV // Phys. Rev. D. 2001. V. 64. P. 032002.

64. *Acosta D. et al. (CDF Collab.).* Measurement of the $t\bar{t}$ Production Cross Section in $p\bar{p}$ Collisions at $\sqrt{s} = 1.96$ TeV // Phys. Rev. Lett. 2006. V. 97. P. 082004.

65. *Abazov V. M.* Helicity of the W Boson in Lepton + Jets $t\bar{t}$ Events // Phys. Lett. B 2005. V. 617. P. 1;
Kondo K. Dynamical Likelihood Method for Reconstruction of Events with Missing Momentum. I. Method and Toy Models // J. Phys. Soc. Japan. 1998. V. 57. P. 4126;
Kondo K. Dynamical Likelihood Method for Reconstruction of Events with Missing Momentum. II. Mass Spectra for 2→2 Processes // J. Phys. Soc. Japan. 1991. V. 60. P. 836;
Dalitz R. H., Goldstein G. R. Decay and Polarization Properties of the Top Quark // Phys. Rev. D. 1992. V. 45. P. 1531.

66. *Berends F. A., Giele W. T., Kuijf H.* Exact Expressions for Processes Involving a Vector Boson and Up to Five Partons // Nucl. Phys. B. 1989. V. 321. P. 39.

67. *Lepage G. P.* A New Algorithm for Adaptive Multidimensional Integration // J. Comp. Phys. 1978. V. 27. P. 192.

68. *James F.* MINUIT Function Minimization and Error Analysis. CERN Program Library Long Writeup D506.

69. *Martin A. D. et al.* Parton Distributions and the LHC: W and Z Production // Eur. Phys. J. C. 2000. V. 14. P. 133.

70. *Albajar C. et al.* Search for $B^0 - \bar{B}^0$ Oscillations at the CERN Proton–Antiproton Collider // Phys. Lett. B. 1987. V. 186. P. 247;
Albrecht H. et al. Observation of $B^0 - \bar{B}_0$ Mixing // Ibid. V. 192. P. 245.

71. *Abdallah J. et al. (DELPHI Collab.).* Search for $B_S^0 - \bar{B}_S^0$ Oscillations in DELPHI Using High-p_t Leptons // Eur. Phys. J. C. 2004. V. 35. P. 35;
Abe K. et al. (SLD Collab.). Search for Time-Dependent $B_S^0 - \bar{B}_S^0$ Oscillations Using a Vertex Charge Dipole Technique // Phys. Rev. D. 2003. V. 67. P. 012006;
Heister A. et al. (ALEPH Collab.). Improved Search for $B_S^0 - \bar{B}_S^0$ Oscillations // Eur. Phys. J. C. 2003. V. 29. P. 143.

72. *Abazov V. M. et al. (D∅ Collab.).* Direct Limits on B_S^0 Oscillation Frequency // Phys. Rev. 2006. V. 97. P. 021802; hep-ex/0603029. 2006.

73. *Abulencia A. et al.* Measurement $B_S^0 - \bar{B}_S^0$ Oscillation Frequency // Phys. Rev. Lett. 2006. V. 97. P. 062003.

74. *Abulencia A. et al.* Observation of $B_S^0 - \bar{B}_S^0$ Oscillation // Ibid. P. 242003.

75. *Piedra J.* Determination of Δm_d and Absolute Calibration of Flavor Taggers for the Delta m_s Analysis, in Fully Reconstructed Decays at the CDF Experiment. Ph. D. Thesis. Univ. of Cantabria. Fermilab Report No. FERMILAB-THESIS-2005-27. 2005.

76. *Leonardo N.* Analysis of B_S Flavor Oscillations at CDF. Ph. D. Thesis. Massachusetts Inst. of Tech. Fermilab Rep. FERMILAB-THESIS-2006-18. 2006.

77. *Moser H. G., Roussarie A.* Mathematical Methods for $B^0 \bar{B}^0$ Oscillation Analyses // Nucl. Instr. Meth. A. 1997. V. 384. P. 491.

78. *Acosta D. et al. (CDF Collab.).* Measurement of Bottom-Quark Hadron Masses in Exclusive J/ψ Decays with the CDF Detector // Phys. Rev. Lett. 2006. V. 96. P. 202001.

79. *Amster C. et al. (PDG).* Review of Particle Physics // Phys. Lett. B. 2008. V. 667. P. 1–1340.

80. *Okamoto M.* CKM Matrix with Lattice QCD — the Full Determination Using Recent Results // Proc. of XXIII Intern. Symposium on Lattice Field Theory. Sci. LAT 2005. Rep. 013; hep-lat/0510113.

81. *Aaltonen T. et al.* Observation of the Heavy Baryons Σ_b and Σ_b^* // Phys. Rev. Lett. 2007. V. 99. P. 202001.

82. *Manohar A. V., Wise M. B.* Heavy Quark Physics // Cambridge Monographs on Particle Physics, Nuclear Physics and Cosmology. V. 10. Cambridge, 2000; and references therein.

83. *Stanly D. P., Robson D.* Do Quarks Interact Pairwise and Satisfy the Color Hypothesis? // Phys. Rev. Lett. 1980. V. 45. P. 235;
Izatt D., DeTar C., Stephenson M. Spectroscopy of Hadrons Containing One Heavy Quark // Nucl. Phys. B. 1982. V. 199. P. 269;

Richard J. M., Taxil P. Baryons with Charm and Strangeness in Potential Models // Phys. Lett. B. 1983. V. 128. P. 453;
Basdevant J. L., Boukraa S. Baryon Masses in Relativistic Potential Models // Z. Phys. C. 1986. V. 30. P. 103;
Hwang W. Y. P., Lichtenberg D. B. Mass Splitting of Heavy Baryon Isospin Multiplets // Phys. Rev. D. 1987. V. 35. P. 3526;
Martin A., Richard J. M. Beautiful and Other Heavy Baryons Revisited // Phys. Lett. B. 1987. V. 185. P. 426.

84. *Jenkins E.* Heavy Baryon Masses in the $1/m_Q$ and $1/N_c$ Expansions // Phys. Rev. D. 1996. V. 54. P. 4515;
Jenkins E. Update of Heavy Baryon Mass Predictions // Phys. Rev. D. 1997. V. 55. P. 10.

85. *Albertus C. et al.* Charmed and Bottom Baryons: A Variational Approach Based on Heavy Quark Symmetry // Nucl. Phys. A. 2004. V. 740. P. 333;
Capstick S. Isospin Violations in Baryons and the Σ_c^0–Σ_c^{++} Mass Difference // Phys. Rev. D. 1987. V. 36. P. 2800.

86. *Roncaglia R., Lichtenberg D. B., Predazzi E.* Predicting the Masses of Baryons Containing One or Two Heavy Quarks // Phys. Rev. D. 1995. V. 52. P. 1722;
Karliner M., Lipkin H. J. The Constituent Quark Model Revisited — Quark Masses, New Predictions for Hadron Masses and KN Pentaquark. hep-ph/0307243.

87. *Bowler K. C. et al. (UKQCD Collab.).* Heavy Baryon Spectroscopy from the Lattice // Phys. Rev. D. 1996. V. 54. P. 3619;
Mathur N., Lewis R., Woloshyn R. M. Charmed and Bottom Baryons from Lattice Nonrelativistic QCD // Phys. Rev. D. 2002. V. 66. P. 014502.

88. *Rosner J. L.* Improved Tests of Relations for Baryon Isomultiplet Splittings // Phys. Rev. D. 1998. V. 57. P. 4310;
Rosner J. L. Mass Splittings in Σ_b and Σ_b^* // Phys. Rev. D. 2007. V. 75. P. 013009;
Karliner M. The Quark Model and b Baryons // Ann. Phys. 2009. V. 324, Iss. 1. P. 2–15; arXiv:0706.2163v5.

89. *Korner G., Kramer M., Pirjol D.* Heavy Baryons // Prog. Part. Nucl. Phys. 1994. V. 33. P. 787.

90. *Lange D. J.* The EvtGen Particle Decay Simulation Package // Nucl. Instr. Meth. A. 2001. V. 462. P. 152.

91. *Royall R.* On the Probability of Observing Misleading Statistical Evidence (with discussion) // J. Am. Statist. Assoc. 2000. V. 95. P. 760.

92. *Buskulic D. et al. (ALEPH Collab.).* Strange b Baryon Production and Lifetime in Z Decays // Phys. Lett. B. 1996. V. 384. P. 449;
Abreu P. et al. (DELPHI Collab.). Production of Strange B Baryons Decaying into $\Xi^{\mp} - \ell^{\mp}$ Pairs at LEP // Z. Phys. C. 1995. V. 68. P. 541;
Abdallah J. et al. (DELPHI Collab.). Production of Ξ_c^0 and Ξ_b in Z Decays and Lifetime Measurement of Ξ_b // Eur. Phys. J. C. 2005. V. 44. P. 299–309.

93. *Abazov V. M. et al. (DØ Collab.).* Direct Observation of the Strange b Baryon Ξ_b^- // Phys Rev. Lett. 2007. V. 99. P. 052001; arXiv:0706.1690 v2.

94. *Aaltonen T. et al. (CDF Collab.).* Observation and Mass Measurement of the Baryon Ξ_b^- // Phys Rev. Lett. 2007. V. 99. P. 052002; hep-ex/0707.0589v2. 2007.

95. *Abulencia A. et al. (CDF Collab.).* Search for Exotic $S = -2$ Baryons in $p\bar{p}$ Collisions at $\sqrt{s} = 1.96$ TeV // Phys. Rev. D. 2007. V. 75. P. 032003.

96. *Nason P., Dawson S., Ellis R. K.* The Total Cross Section for the Production of Heavy Quarks in Hadronic Collisions // Nucl. Phys. B. 1988. V. 303. P. 607;
The One-Particle Inclusive Differential Cross Section for Heavy Quark Production in Hadronic Collisions // Nucl. Phys. B. 1989. V. 327. P. 49.

97. *Peterson C. et al.* // Scaling Violations in Inclusive e^+e^- Annihilation Spectra // Phys. Rev. D. 1983. V. 27. P. 105.

98. *Brun R. et al.* GEANT Detector Description and Simulation Tool. CERN Reports No. CERN-DD-78-2-REV and No. CERN-DD-78-2.